MIT Open Access Articles

How Coalescing Droplets Jump

How Coalescing Droplets Jump

Ryan Enright[1,§,*], Nenad, Miljkovic[2,3], James Sprittles[4], Kevin Nolan[1], Robert Mitchell[5,†] and Evelyn N. Wang[2,*]

[1]*Thermal Management Research Group, Efficient Energy Transfer (ηET) Dept., Bell Labs Ireland, Alcatel-Lucent Ireland Ltd., Blanchardstown Business & Technology Park, Snugborough Rd. Dublin 15, Ireland*
[2]*Department of Mechanical Engineering, Massachusetts Institute of Technology, 77 Massachusetts Avenue, Cambridge, Massachusetts, 02139, USA*
[3]*Department of Mechanical Science and Engineering, University of Illinois, Urbana, Illinois, 61801, USA*
[4]*Mathematics Institute, University of Warwick, Coventry, CV4 7AL, UK*
[5]*Department of Materials Science and Engineering, Massachusetts Institute of Technology, 77 Massachusetts Avenue, Cambridge, Massachusetts, 02139, USA*
[§]*Work initiated while affiliated with* [2] *and Stokes Institute, University of Limerick, Ireland*
[†]*Current address: Intel Corp., 5200 NE Elam Young Parkway, m/s RA3-301, Hillsboro, Oregon 97124, USA.*

*Address correspondence to ryan.enright@alcatel-lucent.com and enwang@mit.edu

Abstract

Surface engineering at the nanoscale is a rapidly developing field that promises to impact a range of applications including energy production, water desalination, self-cleaning and anti-icing surfaces, thermal management of electronics, microfluidic platforms, and environmental pollution control. As the area advances, more detailed insights of dynamic wetting interactions on these surfaces are needed. In particular, the coalescence of two or more droplets on ultra-low adhesion surfaces leads to droplet jumping. Here we show, through detailed measurements of jumping droplets during water condensation coupled with numerical simulations of binary droplet coalescence, that this process is fundamentally inefficient with only a small fraction of the available excess surface energy ($\lesssim 6\%$) convertible into translational kinetic energy. These findings clarify the role of internal fluid dynamics during the jumping droplet coalescence process and underpin the development of systems that can harness jumping droplets for a wide range of applications.

KEYWORDS: nanostructured surface design, coalescence, droplet jumping, microfluidics, condensation, wetting, superhydrophobic

When two or more droplets coalesce on a ultra low adhesion nanostructured surface, the resulting droplet can jump away from the surface in a process that has been termed "coalescence-induced droplet jumping".[1–6] Droplet jumping has recently received significant attention due its fundamental relevance in understanding dynamic droplet processes,[7–19] evolved surface structures found in nature,[20] and surface-charge separation.[3] Jumping droplets have also been used to enhance performance in a variety of applications including condensation heat transfer,[2,21–23] self-cleaning surfaces,[24] thermal diodes,[25,26] anti-icing surfaces,[6,27,28] and energy harvesting.[29] Beyond these demonstrated applications, droplet jumping also has potential for use in thermally-driven water desalination systems,[30] in combination with acoustophoretic droplet manipulation to realize novel microfluidic platforms[31] and in mitigating environmentally polluting gas and particle emissions by providing a convenient waste-heat-driven source of microscopic water droplets for wet scrubbing systems.[32]

At the basic level, droplet jumping is a process governed by the conversion of excess surface energy into kinetic energy when two or more droplets coalesce[7,33] and involves a symmetry-breaking surface.[8] For the simplest case of two, equally-sized inviscid spherical droplets coalescing on a surface with no adhesion, an energy-balance gives a characteristic jumping speed that follows an inertial-capillary scaling[7]

$$U \sim \sqrt{\gamma/\rho R}, \tag{1}$$

where R, γ and ρ are the initial radii, surface tension and density of the droplets, respectively. Previous water condensation experiments on a hierarchical superhydrophobic surface have shown an approximately constant scaled jumping speed of $\approx 0.2U$ for jumping droplets with diameters larger than ≈ 100 μm. For smaller diameters, jumping speeds rapidly decreased with no droplet jumping observed below diameters of ≈ 20 μm.[7] Several subsequent studies have attempted to explain these observations by adding terms to the energy-balance approach to account for viscous dissipation, surface adhesion effects and participating velocity components,[9,13,16] but have demonstrated limited success. While a recent numerical simulation replicated experimental observations,[1] this study was limited to a single droplet

diameter. Despite the significant research efforts, there continues to be a lack of quantitative experimental data characterizing droplet jumping and the precise mechanism governing droplet jumping remains not well-understood.

In this work, we studied the process of coalescence-induced droplet jumping over a wide parameter space using a combination of water condensation experiments on nanostructured superhydrophobic surfaces and detailed numerical simulations. In order to experimentally isolate the fundamental energy conversion process associated with droplet jumping, we fabricated surfaces demonstrating *apparent* contact angles approaching 180° and almost zero contact angle hysteresis, thus mitigating the influence of surface adhesion.[4,11] Using high-speed imaging, we measured droplet-jumping speeds normal to the condensing surface as high as 1.4 m/s for jumping droplet diameters as small as ≈ 10 μm. However, while the measured velocities were up to approximately six times larger than the highest velocities previously reported,[7,9] they were still approximately one-fifth of the speed indicated by Eq. (1).

Meanwhile, using 2D axisymmetric numerical simulations, we obtained detailed information of the internal flow momentum generated during droplet coalescence. By recognizing that only unbalanced momentum components can contribute to droplet translational motion, a fact neglected in the derivation of Eq. (1), we found that coalescence-induced droplet jumping is an inherently *inefficient* process with only a small fraction of the available excess surface energy ΔE ($\lesssim 6\%$) being converted to *useful* internal flow momentum to provide the jumping droplet with translational kinetic energy E_j, *i.e.*, $\eta_j = E_j/\Delta E \lesssim$ 0.06.Contrary to previous conclusions drawn from theoretical estimates,[9,13] we found that internal viscous dissipation plays a limited role in the jumping process for the experimentally accessible low Oh number regime studied ($Oh = \mu/\sqrt{\rho\gamma R} \lesssim 0.1$, where μ is the droplet dynamic viscosity).[34] With our developed understanding, we determined a dimensionless droplet-size-dependent correction to Eq. (1) that demonstrated good agreement with our experimental data. Our results elucidate the coupled nature of

3

surface-mediated symmetry breaking and the internal flow momentum on jumping droplet dynamics. Furthermore, our mechanistic framework provides a starting point for more detailed analysis involving complicating factors such as finite surface adhesion, unequal coalescing droplet geometries and complex surface architectures.

RESULTS AND DISCUSSION

Experiments. To minimize the influence of the underlying substrate on the droplet jumping process, we prepared fluoropolymer-coated carbon nanotube (CNT)-based superhydrophobic surfaces with a structure spacing length scale of $l \sim 100$ nm that was much smaller than the typical jumping droplet radius ($l/R \sim 0.01 \ll 1$) (see Methods). The coated CNTs had typical diameters of $d \approx 40$ nm (Figure 1a) and atomic force microscopy scans of the surface in soft tapping mode showed a maximum height variation of 820 nm, consistent with the height measured from scanning electron microscope images of the surface (Figure 1b). Measurements of the advancing macroscopic contact angle demonstrated highly non-wetting behavior, $\theta_a^{app} = 170.2° \pm 2.4° \left(\cos\theta_a^{app} = -0.985 \approx -1\right)$ (Figure 1c). Moreover, the measured contact angle hysteresis of macroscopic droplets was found to be small ($\Delta\cos\theta = \cos\theta_{app}^a - \cos\theta_{app}^r = -0.0154 \approx 0$). Condensed droplets with diameters as small as 2 µm demonstrated large apparent contact angles (Figure 1d) similar to the macroscopically measured value (Figure 1e). A conservative estimate of the droplet radius-dependent advancing angle, $\theta_a^{app}(R)$, indicated that all measured droplet jumping events were in a constant contact angle growth mode.[4] We also fabricated and tested fluoropolymer-coated CuO nanostructures, which we have previously shown to demonstrate good jumping droplet behavior,[2–4] with macroscopic advancing contact angle and contact angle hysteresis behavior similar to that of the functionalized CNT surfaces (see Methods). Since the characteristic roughness spacing length scales of the surfaces ($l \approx 0.1 - 1$ µm) were significantly smaller than the smallest droplet jumping diameter measured (≈ 10 µm), we were able access a droplet growth regime well above the flooding limit with droplets growing in a constant *apparent* contact angle mode.[2,4,5] Since the work of adhesion scales as

$W \propto (1 + \cos\theta)$, the contact angle measurements suggested that the effect of surface adhesion on the droplet jumping process could be neglected.

Condensation experiments were carried out under humid atmospheric conditions using a two-camera arrangement and in a pressure-regulated environmental chamber using a single-camera arrangement (see Methods, supporting information S2 – S4). In the former experimental set-up, an overhead CCD camera was used to capture images of the droplets prior to coalescence to provide the initial conditions, *i.e.*, the droplet radii and number of droplets involved in the jumping event. Knowledge of these initial conditions allowed us to isolate binary droplet jumping events for droplets of equal radii with near surface-normal trajectories that maximized the jumping velocity.[7,11] The latter experimental set-up allowed us to study droplet jumping at condensing surface temperatures higher than the laboratory ambient conditions and under varying gas densities to rule out the possibility that external drag plays a significant role during the droplet coalescence process before jumping, as assumed in our numerical simulations. In both experimental set-ups, a high-speed camera was used to capture the out-of-plane jumping droplet trajectory.

Figure 2a shows representative time-lapse images capturing a jumping droplet following the coalescence of two equally sized droplets ($R \approx 19.5$ µm) obtained using the two-camera arrangement. The center of the streak was taken as the average y position of the jumping droplet in each frame relative to the initial location of the droplets on the condensing surface ($y = 0$), while the average velocity of the jumping droplet was found by measuring the length of the streak and dividing this by the shutter speed of the camera. These two measures together defined the experimental trajectory of the jumping droplets. To obtain an accurate estimate of the jumping velocity associated with the converted excess surface energy, the theoretical droplet trajectory was calculated (see supporting information S5).

In Figure 2b the theoretical trajectory is shown fitted to the experimental data to determine the droplet jumping velocity as it departed the surface. Based on the fitted trajectory, we determined a

jumping velocity of $v_j = 0.41\pm0.01$ m/s (inset of Figure 2b), which was 0.21× the characteristic jumping speed given by the capillary-inertial scaling, $U \approx \sqrt{\gamma/(\rho R)} = 1.92$ m/s (Figure 2c). This result was generally repeatable over a number of experiments for a wide range of droplet sizes and is consistent with the previously identified size-independent region.[7] In order to better understand the reason for jumping velocity magnitudes significantly smaller than those given by Eq. (**1**) in view of the ultra-low surface adhesion characteristic of the condensing surfaces in our study, we considered the nature of the droplet coalescence process and performed numerical simulations to determine the jumping velocity in the absence of surface adhesion effects. Analysis of the simulations improved our understanding of how the excess surface energy was transferred to the translational kinetic energy of the jumping droplet by considering the details of the internal flow developed during the coalescence process.

Theory & Simulations. A schematic of the coalescence process for two, equally-sized, condensed droplets defined by a radius, R, resting on a surface characterized by $\theta_a^{app} \to 180°$ and $\Delta\cos\theta \to 0$ is shown in Figure 3a. Soon after the interfaces of the two droplets make contact, a liquid bridge develops that is accelerated radially from the point of contact due to the curvature difference (in the longitudinal direction) between the bridge radius ($1/r_b$) and the droplets ($1/R$). Initially, viscous forces control the bridge flow dynamics. However, inertia begins to dominate the flow dynamics when the bridge radius, r_b, exceeds the critical bridge radius $r_c = 64\mu^2/(\rho\gamma C^4)$,[34,35] where C is a constant previously determined from simulation[36] and experimental measurement[35,37,38] to have a value ranging between 1.39 and 1.62. For water at ambient conditions and based on the range of C, $r_c \approx 165 - 311$ nm. Considering the inertial regime, scaling of the bridge flow yields a time-varying bridge radius $r_b(t)$ formed during coalescence given by[36,39]

$$r_b = CR\sqrt{t/\tau},$$

(2)

where $\tau = \sqrt{\rho R^3/\gamma}$ is the inertial-based time scale of the coalescence process. Differentiating Eq. (2) with respect to time gives

$$v_b = \frac{1}{2}\frac{CR}{\sqrt{\tau t}}. \tag{3}$$

Noting the definition of τ, Eq. (3) shows that $v_b \sim \sqrt{\gamma/(\rho R)}$; corresponding to the scaling given by Eq. (**1**). This equivalence between the energy state scaling and the scaling behavior of the radial bridging flow highlights the link between the jumping droplet speed and the excess surface energy being transferred to the internal flow during the coalescence process. Specifically, by considering the symmetry of the system, we seek to relate the internal flow to the jumping of the droplet from the surface by finding the momentum component of the internal flow normal to the symmetry-breaking surface, *i.e.*, *y*-coordinate in Figure 3a. Due to symmetry considerations, the other two momentum components parallel to the surface (*x*- and *z*-coordinates) give zero net momentum before and after the impact of the bridging flow on the surface.

To determine the *y*-component of momentum, p_y, generated during the coalescence process, 3D axisymmetric numerical simulations were performed using a finite-element code specifically designed to accurately model unsteady micro-capillary flows in which both viscous and inertial forces are present in the liquid. This code has previously been shown to accurately capture the coalescence process[40], and was originally developed for dynamic wetting flows[41] (see Methods).

In Figure 3b-f, the numerically simulated flow field of the coalescence process for $Oh = 0.012$ ($r_c/R = 64Oh^2/C^4 \approx 2\times10^{-3}$), corresponding to water droplets at approximately ambient conditions with initial radii of $R = 100$ μm, and $0.25 \le r_b/R \le 2^{1/3}$ is shown in terms of the radial velocity component, u_r, and the flow streamlines (see supporting information S6 for flow fields obtained for larger Oh). In the early stages of coalescence ($r_b/R = 1/4$), flow enters the expanding liquid bridge from the droplet bulk near the bridge due to the low pressure region generated by the large longitudinal bridge curvature.[39] The bridging process generates a capillary wave (Figure 4a) that propagates along the interface away from the bridge region. The local pressures associated with the capillary wave fluctuate above and below the initial equilibrium pressure. As the capillary wave propagates and disperses (Figure 4b-d), there is a corresponding expansion in both the positive and negative components of the radial velocity (Figure 3c-

e). Beyond $r_b/R = 1$, the negative radial flow decays until, at $r_b/R = 2^{1/3}$ (Figure 3f), the radial flow component is positive everywhere. This result corresponds to a relatively large pressure fluctuation as the capillary wave reaches the end of the droplet and is reflected back towards the coalescence symmetry plane. This increase in pressure, as well as the inertia already obtained, generates a flow with a significant positive radial component (Figure 3f).

Also shown in Figure 4 are the capillary wave characteristics for larger Oh values of 0.037 ($r_c/R \approx 2 \times 10^{-2}$) and 0.118 ($r_c/R \approx 0.13 - 0.24$). As Oh increases, the propagating capillary wave driving the internal flow becomes significantly damped; a consequence of the Oh number representing the dimensionless viscosity. The reduced amplitude of the pressure fluctuations with respect to the initial equilibrium pressure along with increased viscous dissipation within the droplet leads to a characteristic change in both the interface shape evolution and internal flow field of the coalescing droplet (see supporting information S6). As we show later, this behavior correlates with the magnitude of the internal flow momentum generated during coalescence to give an Oh-dependent jumping velocity.

The change in droplet shape evolution and internal flow field was reflected in the cumulative viscous dissipation of the flow during the coalescence process, $E_d(r_b/R)$, normalized by the available excess surface energy budget, ΔE, shown in Figure 5a. As expected, an increasing proportion of the excess surface energy budget was consumed by viscous losses with increasing Oh. Figure 5b shows the normalized viscous dissipation evaluated from our simulations at $r_b/R = 2^{1/3}$ as a function of Oh and previous estimations.[9,13] The dissipation estimates are seen to either under predict or over predict the viscous losses compared to our simulations. More importantly though, both estimates predict a linear increase in viscous dissipation with increasing Oh, which is due to the fact that only a single inertial timescale was used to characterize droplet coalescence for all Oh.[9,13] The simulation results, however, show a decreasing rate of viscous dissipation growth with increasing Oh. This can be understood by considering the limiting case of very large Oh where the normalized viscous dissipation must asymptote to unity when evaluated up to $r_b/R = 2^{1/3}$ resulting in a smooth transition to a sphere during coalescence.[40] As we show next, simply adding a viscous dissipation term into the energy-balance analysis cannot

capture the subtle effect of viscosity on the development of the internal flow momentum component

normal to the condensing surface with varying *Oh*.

To extract the *y*-component (surface-normal) of momentum from the simulations, we considered

axisymmetric motion about the *z*-axis of a cylindrical coordinate system (r, z, β) for $z > 0$ due to the

symmetry between the two coalescing drops. The velocity component perpendicular to the surface is

$u_y = u_r \sin \beta$, where u_r is the velocity in the radial direction and β is the azimuthal coordinate.

Accordingly, the momentum perpendicular to the surface in the *upper half* of the two coalescing droplets

is

$$p_y = 2\rho \iint_0^\pi r u_r \sin \beta \, d\beta dr dz. \tag{4}$$

The first integral in Eq. (4) gives the *y*-component of the radial velocity, while the second integral

operates over the *r-z* plane. The total momentum given by Eq. (4) can be further broken down into

positive, p_y^+, and negative, p_y^-, contributions to p_y depending on whether the associated radial flow is

moving away from or towards the *z*-axis.

Figure 5c shows the *y*-components of the momentum extracted from the numerical simulations

non-dimensionalised by the characteristic momentum of the system, $m_j U$, for $Oh = 0.012$, 0.037 and

0.118. The results are compared to the prediction of a simple model description of the *y*-component of the

bridging flow momentum in the inertial limit (see supporting S7 for derivation) given by

$$\left. \frac{p_y^+\big|_{r_b/R \lesssim 1}}{m_j U} = \frac{3}{2\pi} C^2 \left(\frac{r_b}{R}\right)^3. \tag{5}$$

Despite the simplified nature of our analysis, we find that a numerical prefactor of $C = 1.3$ inserted into

Eq. (5) provides good agreement with the simulated p_y^+ up to $r_b/R \approx 1$ for the smallest simulated *Oh*.

This serves to highlight the dominant role of the bridging flow in generating internal flow momentum at

this stage of the coalescence process.

For $Oh = 0.012$ and $r_b/R \gtrsim 1$, we observed a distinct reduction in the growth of the numerically

simulated p_y^+ coinciding with positive radial flow spreading to the entire droplet and the commensurate

decay of the negative radial flow (Figure 3e & f) that can be observed in Figure 5c in terms of the negative momentum, p_y^-, that reached a minimum at $r_b/R \approx 1$ before returning to zero. The dwell in the positive momentum growth was followed by a high rate of growth that was approximately three orders faster ($\sim (r_b/R)^6$) than during the bridge phase ($r_b/R \lesssim 1$) and reached a maximum at $r_b/R \approx 2^{1/3}$. This large increase in p_y^+ corresponds to the entirely positive radial flow observed in Figure 3f. Beyond this point in our simulations, p_y^+ began to decay due to the inherent symmetry of the simulated system with energy being stored in the stretched interface as the momentum of the flow carried the bridge radius past the final equilibrium position of $r_b/R = 2^{1/3}$. However, due to the breaking of symmetry by the condensing surface, in our experiments this excess momentum at $r_b/R \approx 2^{1/3}$ is unbalanced and can contribute directly to the momentum of the jumping droplet. Note that, for the analysis performed here, we have defined the excess momentum as the maximum momentum at $r_b/R \geq 2^{1/3}$. This provides consistency for the situation where the peak in momentum may occur at $r_b/R < 2^{1/3}$ for Oh numbers larger than those simulated here and in the viscous limit ($r_c/R \gtrsim 1$) where we expect all momentum in the system to tend to zero as $r_b/R \rightarrow 2^{1/3}$.

As Oh was increased in the simulations, the momentum growth rate in the bridge phase slowed down and the characteristic kink in momentum growth beyond $r_b/R = 1$ observed for smaller Oh ($= 0.012$) was smoothed out. This corresponded with a reduction in the excess momentum obtained at $r_b/R \approx 2^{1/3}$ and a shift to smaller values of r_b/R where the maximum momentum occurred. In the p_y^- region, the minimum found at $r_b/R \approx 1$ for low Oh shifted to smaller values of r_b/R and decreased in magnitude. The change in momentum generated with increasing Oh is consistent with the coalescence dynamics moving into the transition region between the inertially and viscously-dominated coalescence regimes as $r_c/R \rightarrow 1$.[35]

To complete the picture of flow momentum available for droplet jumping, we considered the lower region of the coalescing droplets ($y < 0$) where the sign of the momentum components are reversed. Distinct from the upper region ($y > 0$), the bridging flow interacts with the condensing surface. At the

moment when the bridge impacts the surface ($r_b/R \approx 1$), the flow in the negative y-direction has a

momentum $-p_y^+\big|_{r_b/R=1}$. The bridge impact develops a region of high pressure as the dynamic pressure of

the flow is converted to static pressure[1], imposing a force on the liquid and the interface. For simplicity,

we assumed that the flow momentum induced by this pressure is equal, but opposite, to the momentum in

the negative y-direction just prior to impact, $p_y^+\big|_{r_b/R=1}$. We also considered the contribution to the y-

component of momentum of the internal flow in the flow neighboring the bridge, $-p_y^-\big|_{r_b/R=1}$. While

detailed analysis of 3D simulations are required to confirm these assumptions, we can bound the

momentum available for jumping by $p_y^+\big|_{\max(r_b/R \geq 2^{1/3})}$ and $2p_y^+\big|_{\max(r_b/R \geq 2^{1/3})}$. Verification that the

experimental data lay between these bounds will support our developed approach, with the specific

expression derived below as a starting point for a more complex description of the full three-dimensional

dynamics.

Next, we balanced the y-momentum of the coalescing droplet system by summing the three

identified y-components of momentum generated by the internal flow and compared them to the total

momentum of the jumping droplet,

$$\sum p_y/(m_j U) = \left(p_y^+\big|_{r_b/R=1} + p_y^+\big|_{\max(r_b/R \geq 2^{1/3})} - p_y^-\big|_{r_b/R=1} \right)/(m_j U) = \frac{v_j}{U}. \tag{6}$$

In Figure 5d, $p_y^+\big|_{\max(r_b/R \geq 2^{1/3})}/(m_j U)$ and the summation of contributing momentum y-components

given by Eq. (6) are plotted as a function of the Oh number. As Oh increases, there is an approximately

linear decrease in available internal flow momentum for droplet jumping ($\sum p_y/(m_j U) \sim -Oh$),

resulting in an approximately 2× reduction in dimensionless jumping velocity as Oh increases from 0.01

to 0.12. In addition, the $p_y^+\big|_{\max(r_b/R \geq 2^{1/3})}/(m_j U)$ term contributes two-thirds of the momentum to the

jumping process, $\approx 67\%$, over the range of Oh simulated (see Figure 5d and supporting information S8)

with the remainder of the contributing momentum originating from the bridge impact region.[1] A fit to the

numerical data resulted in the following expression for the jumping velocity

$$v_j = (3.4026Oh^2 - 1.5285Oh + 0.2831)U$$

<div align="right">(7)</div>

(see supporting information S9 for fit statistics). Towards the inviscid limit ($Oh\rightarrow0$), the jumping velocity

is $v_j \approx 0.28U$. Calculating the kinetic energy of the jumping droplet based on this velocity and comparing

to the available excess surface energy in the system (ΔE), only $\approx 6\%$ of the excess surface energy budget

was converted to the translational kinetic energy of the jumping droplet (E_j). As Oh increased, the energy

conversion efficiency ($\eta_j = E_j/\Delta E$) decreased further reaching $\eta_j \approx 1.8\%$ for $Oh = 0.12$ (see supporting

information S10). Interestingly, the conversion efficiencies of coalescence-induced droplet jumping are

characteristically smaller than that of a solid disc transitioning to a sphere as it melts, where $\eta_j \approx 20\%$

have been found.[17] This characteristically larger η_j further highlights the importance of the internal flow

momentum developed during the capillary-driven jumping process, which is intimately linked to the

initial geometry of the system. Next, we compared the results of the numerical simulations to the

experimentally measured jumping velocities.

Comparison to experiment. In Figure 6a & b, our experimentally measured droplet jumping velocities

and the predictions of our numerical simulations (Eq. (6) & Figure 5d) are plotted as a function of the

jumping droplet diameter, $2R_j$. Also shown in Figure 6a is a previously obtained experimental data set.[7]

For experiments performed under low pressure in the environmental chamber (Figure 6b), where vapor

density was reduced, but viscosity remained approximately unchanged ($Re \leq 1$), a simple linear fit was

applied to the measured droplet trajectory to determine the jumping speed due to the potential for

molecular slip effects on the drag force. Unlike the two-camera arrangement (Figure 6a), the initial

conditions before coalescence were difficult to ascertain using a single-camera arrangement (Figure 6b),

especially with decreasing droplet radii. However, we classified jumping events based on the angular

deviation of the droplet trajectories from the surface normal, rejecting jumping events deviating more

than 5° from the normal. Also rejected from the analysis were droplet jumping events triggered by

incoming droplets (see supporting information S1 for movie details).[7,9] In general, data obtained from the

one-camera arrangement showed more scatter due to our inability to completely filter coalescing droplets with non-equal radii and jumping events triggered by more than two droplets.

We demonstrated excellent agreement between our numerical predictions and experimental data with the latter well-bounded by the limits placed on the jumping speed by $p_y^+|_{\max(r_b/R \geq 2^{1/3})}$ and $2p_y^+|_{\max(r_b/R \geq 2^{1/3})}$, giving us confidence in our interpretation of the physics. In addition, we found that the data measured using the two-camera arrangement, which removes the ambiguity surrounding the initial coalescence conditions associated with the one-camera arrangement, followed the numerical predictions exceptionally well. Indeed, for the experiment presented in Figure 2 using the two-camera arrangement, the numerical simulations predicted $v_j = 0.23U$, which was within 10% of the experimental jumping velocity of $v_j \approx 0.21U$. For the one-camera arrangement, we measured jumping speeds as high as 1.4 m/s, approximately 6× larger than previously reported[7], due to a combination of the elevated temperature of the environmental chamber with respect to ambient and the smaller jumping droplet diameters allowed by our nanostructured surfaces. Experiments performed in the environmental chamber also confirmed that the surrounding gas pressure played no role on the jumping speed (see supporting information S11).

Interestingly, previous experimental data are well-captured by our numerical results without the need to introduce a surface adhesion term for $2R_j > 100$ µm,[7] indicating that droplets in this size range had reached a constant contact angle growth wetting state characterized by macroscopic contact angle measurements on this surface, $\theta \approx 170°, \Delta\theta \approx 0°$.[42] However, for droplets smaller than 100 µm, there was an increasing discrepancy in comparison to our numerical results. While it has previously been suggested that the observed peak and then decreasing jumping speed with decreasing droplet size arises as a result of internal viscous dissipation,[7,9,13,43] the jumping speeds fall off faster than our experimental and numerical data in this range of *Oh* (Figure 6c). This observation implicates a surface interaction mechanism rather than a fundamental hydrodynamic limitation and highlights that the details of the

13

evolving droplet morphology need to be carefully considered when interpreting experimental data of droplet jumping. Indeed, complex wetting interactions associated with condensed droplet growth on hierarchical surfaces have been shown to influence the ability of coalescing droplets to jump,[10] a fact not captured in our present analysis. However, we believe that the mechanistic framework we have developed to understand droplet jumping can be readily extended to deal with these non-idealities.

CONCLUSIONS

In summary, we demonstrated experimentally and numerically that coalescence-induced droplet jumping on ultra-low adhesion surfaces is fundamentally inefficient. Through the use of detailed measurements of jumping droplets during water condensation coupled with numerical simulations of binary droplet coalescence, we have elucidated that only a small fraction of the excess surface energy ($\leq 6\%$) is convertible into translational kinetic energy. These findings clarify the role of internal fluid dynamics during the jumping droplet coalescence process and underpin the development of systems that can harness jumping droplets for a wide range of applications. Furthermore, this work offers fundamentally new insight into the process of coalescence-induced droplet jumping and has defined a fundamental upper bound for jumping speeds on flat non-wetting surfaces.

Methods

Surface synthesis. Carbon nanotubes were grown by chemical vapor deposition (CVD) [44]. Silicon growth substrates were prepared by sequentially depositing a 20 nm thick Al_2O_3 diffusion barrier and a 5 nm thick film of Fe catalyst layer using electron-beam deposition. Growth was performed in a 2.54 cm quartz furnace tube. Following a 15 min purge in a H_2/He atmosphere, the growth substrate was annealed by ramping the furnace temperature to 750 °C followed by a 3 minute anneal at temperature, while maintaining a flow of H_2 and He at 400 sccm and 100 sccm, respectively. CNT growth was then initiated by flowing C_2H_4 at 200 sccm. The flow of C_2H_4 was stopped after a period of 1 minute. The thermally-grown CNT had a typical outer diameter of $d \approx 7$ nm. Due to the short growth time (~5 min.) the CNT did not form a well-aligned forest, but rather a tangled turf.

To create the CuO nanostructures, commercially available oxygen-free Cu tabs (20 mm x 2 mm x 1 mm) were used (99.9 % purity), as the test samples for the experiments. Each Cu tab was cleaned in an ultrasonic bath with acetone for 10 minutes and rinsed with ethanol, isopropyl alcohol and de-ionized (DI) water. The tabs were then dipped into a 2.0 M hydrochloric acid solution for 10 minutes to remove the native oxide film on the surface, then triple-rinsed with DI water and dried with clean nitrogen gas. Nanostructured CuO films were formed by immersing the cleaned tabs into a hot (96 ± 3 °C) alkaline solution composed of $NaClO_2$, NaOH, $Na_3PO_4 \cdot 12H_2O$, and DI water (3.75 : 5 : 10 : 100 wt.%) [45]. During the oxidation process, a thin ($\approx$300 nm) Cu_2O layer was formed that then re-oxidized to form sharp, knife-like CuO oxide structures with heights of $h \approx 1$ μm, solid fraction $\varphi \approx 0.023$ and roughness factor $r \approx 10$.

To functionalize the surfaces, a proprietary fluorinated polymer was deposited using plasma enhanced vapor deposition (P2i). The process occurs under low pressure within a vacuum chamber at room temperature. The coating is introduced as a vapor and ionized. This process allows for the development of a highly conformal ($\approx$ 30 nm thick) polymer layer, which forms a covalent bond with the surface, making it extremely durable. Goniometric measurements (Kyowa Interface Science Ltd., MCA-3) of $\approx$100 nL droplets on a smooth P2i coated silicon wafer surface showed advancing and receding contact angles of θ_a = 124.3° ± 3.1° and θ_r = 112.6° ± 2.8°, respectively. Using the values of the advancing angles on the rough and smooth P2i surfaces, we estimated the effective solid fraction of both the CNT and CuO surfaces to be $\varphi = \left(\cos \theta_a^{app} + 1 \right)/(\cos \theta_a + 1) \approx 0.03$.

Jumping droplet experiments. Condensation experiments carried out under humid atmospheric conditions used two cameras that were orthogonally aligned and focused at the same point in space (MCA-3, Kyowa Interface Ltd.) (see Supporting information S2). An overhead CCD camera was used to capture images of the droplets prior to coalescence to provide the initial conditions. The out-of-plane trajectory of the jumping droplets was captured using a high-speed camera (Photron, Fastcam SA2) at frame capture rates of 5, 7.5 and 18 kHz corresponding to shutter speeds of 185, 133 and 56 μs, respectively. Back illumination was provided by a fiber light positioned behind the sample with respect to the high-speed camera. The experiment was initiated by first cooling the surface to a temperature of $T_w = 5$ °C, corresponding to a local saturation pressure of $p_w = 0.9$ kPa on a cold-stage under a dry N_2 stream. The dry N_2 stream was then shut-off to initiate condensation from the ambient atmosphere with a relative humidity of $\approx$ 55% and a dry-bulb temperature of $\approx$ 20 °C corresponding to a vapor saturation pressure of $p_v \approx 1.28$ kPa and a supersaturation of $S = p_v/p_w \approx 1.42$.

Condensation experiments were also carried out under saturated conditions in a pressure regulated environmental chamber using a single-camera arrangement (see supporting information S3 & S4). The out-of-plane trajectory of the jumping droplets was captured using a high-speed camera (Vision Research, Phantom v7.1) at frame capture rates of 7.2, 10, and 20 kHz corresponding to shutter speeds of 139, 100, and 50 μs, respectively. The camera was mounted outside of the environmental chamber and fitted with an extended macro lens assembly. Illumination was supplied by light emitting diodes installed inside the chamber and providing back lighting to the sample. The sample tabs were mounted to a flattened copper tube connected to an external cooling loop and was maintained at a temperature of $T_w = 26$ °C ($p_w = 3.33$ kPa). The water vapor supply was vigorously boiled before the experiments to remove non-condensable gases. The experiment was initiated by first evacuating the environmental chamber to medium-vacuum levels (=0.5 ± 0.025 Pa). Water vapor was then introduced into the environmental chamber *via* a bellows valve set to maintain the chamber pressure at $p_v = 3.6 ± 0.175$ kPa corresponding to a supersaturation of S ≈ 1.05.

Numerical modeling. A purpose-built finite-element-based computational code was used to capture the dynamics of the coalescence process. The bulk flow of the liquid is governed by the incompressible Navier-Stokes equations whilst the boundary conditions are given by either the conventional model or by the interface formation model, which generalizes the usual boundary conditions for flows in which interfaces are formed or destroyed [46]. In the range of parameter space studied in this paper, the differences in the predictions of the two models for the global dynamics of the drops was small; however, larger differences may be expected when considering smaller drops.

A full description of the models used, benchmark simulations confirming the codes accuracy and a comparison to recent experimental data are provided in ref. [40] Furthermore, a step-by-step user-friendly guide to the development of the code can be found in ref. [47] and the extension to interface formation dynamics is in ref. [41]. Therefore, here we only briefly recapitulate the main details.

The code uses an arbitrary Lagrangian Eulerian approach, so that the free surface dynamics are captured with high accuracy. The mesh is based on the bipolar coordinate system, and is graded so that exceptionally small elements can be placed near the bridge front; consequently, in contrast to many previous works, both local and global physical scales of the coalescence process are properly resolved. Triangular finite elements of V6P3 type are used and the result of our spatial discretization is a system of non-linear differential algebraic equations of index two which are solved using the second-order backward differentiation formula using a time step which automatically adapts during a simulation to capture the appropriate temporal scale at that instant.

Supporting information available
One video showing incoming droplet triggered jumping, as well as further information on the jumping-droplet experiments, data collection methodology, and supplementary analysis. This material is available free of charge *via* the Internet at http://pubs.acs.org.

Author contributions
R.E., N.M. and E.N.W. conceived the initial idea of this research. R.E., R.M. and N.M. fabricated and characterized the experimental samples. R.E. and N.M. carried out the experiments and collected data. R.E. and N.M. analyzed the experimental data. J.S. performed the numerical simulations. R.E., K.N. and J.S. analyzed the numerical data. R.E. carried out the theoretical analysis. R.E. and E.N.W. were responsible for writing the paper. All authors commented on the paper.

Competing financial interests
The authors declare no competing financial interests.

References

(1) Nam, Y. S.; Kim, H.; Shin, S. Energy and Hydrodynamics Analyses of Coalescence-Induced Jumping Droplets. *Appl. Phys. Lett.* **2013**, *103*, 161601.

(2) Miljkovic, N.; Enright, R.; Nam, Y.; Lopez, K.; Dou, N.; Sack, J.; Wang, E. N. Jumping-Droplet-Enhanced Condensation on Scalable Superhydrophobic Nanostructured Surfaces. *Nano Lett.* **2012**, *13*, 179–187.

(3) Miljkovic, N.; Preston, D.; Enright, R.; Wang, E. N. Electrostatic Charging of Jumping Droplets. *Nat. Commun.* **2013**, *4*, 2517, doi:10.1038/ncomms3517.

(4) Enright, R.; Miljkovic, N.; Dou, N.; Nam, Y.; Wang, E. N. Condensation on Superhydrophobic Copper Oxide Nanostructures. *J. Heat Transf.* **2013**, *135*, 091304.

(5) Enright, R.; Miljkovic, N.; Al-Obeidi, A.; Thompson, C. V.; Wang, E. N. Condensation on Superhydrophobic Surfaces: The Role of Local Energy Barriers and Structure Length Scale. *Langmuir* **2012**, *28*, 14424–14432.

(6) Boreyko, J. B.; Collier, C. P. Delayed Frost Growth on Jumping-Drop Superhydrophobic Surfaces. *ACS Nano* **2013**, *7*, 1618–1627.

(7) Boreyko, J. B.; Chen, C. H. Self-Propelled Dropwise Condensate on Superhydrophobic Surfaces. *Phys. Rev. Lett.* **2009**, *103*, 184501.

(8) Boreyko, J. B.; Chen, C. H. Self-Propelled Jumping Drops on Superhydrophobic Surfaces. *Phys. Fluids* **2010**, *22*, 091110.

(9) Lv, C.; Hao, P.; Yao, Z.; Song, Y.; Zhang, X.; He, F. Condensation and Jumping Relay of Droplets on Lotus Leaf. *Appl. Phys. Lett.* **2013**, *103*, 021601.

(10) Rykaczewski, K.; Paxson, A. T.; Anand, S.; Chen, X.; Wang, Z.; Varanasi, K. K. Multimode Multidrop Serial Coalescence Effects During Condensation on Hierarchical Superhydrophobic Surfaces. *Langmuir* **2012**, *29*, 881–891.

(11) He, M.; Zhou, X.; Zeng, X.; Cui, D.; Zhang, Q.; Chen, J.; Li, H.; Wang, J.; Cao, Z.; Song, Y.; *et al.* Hierarchically Structured Porous Aluminium Surfaces for High-Efficient Removal of Condensed Water. *Soft Matter* **2012**, *8*, 6680 – 6683.

(12) He, M.; Zhang, Q.; Zeng, X.; Cui, D.; Chen, J.; Li, H.; Wang, J.; Song, Y. Hierarchical Porous Surface for Efficiently Controlling Microdroplets' Self-Removal. *Adv. Mater.* **2013**, *25*, 2291–2295.

(13) Wang, F.-C.; Yang, F.; Zhao, Y.-P. Size Effect on the Coalescence-Induced Self-Propelled Droplet. *Appl. Phys. Lett.* **2011**, *98*, 053112.

(14) X. Chen, J. W. Nanograssed Micropyramidal Architectures for Continuous Dropwise Condensation. *Adv. Funct. Mater.* **2011**, *21*, 4617–4623.

(15) Feng, J.; Qin, Z.; Yao, S. Factors Affecting the Spontaneous Motion of Condensate Drops on Superhydrophobic Copper Surfaces. *Langmuir* **2012**, *28*, 6067–6075.

(16) Peng, B.; Wang, S.; Lan, Z.; Xu, W.; Wen, R.; Ma, X. Analysis of Droplet Jumping Phenomenon with Lattice Boltzmann Simulation of Droplet Coalescence. *Appl. Phys. Lett.* **2013**, *102*, 151601.

(17) Habenicht, A.; Olapinski, M.; Burmeister, F.; Leiderer, P.; Boneberg, J. Jumping Nanodroplets. *Science* **2005**, *309*, 2043–2045.

(18) Lee, S.; Lee, S.; Kang, K. Jumping of a Droplet on a Superhydrophobic Surface in AC Electrowetting. *J. Vis.* **2011**, *14*, 259–264.

(19) Jun Lee, S.; Lee, S.; Hyoung Kang, K. Droplet Jumping by Electrowetting and Its Application to the Three-Dimensional Digital Microfluidics. *Appl. Phys. Lett.* **2012**, *100*, 081604.

(20) Mockenhaupt, B.; Ensikat, H.-J.; Spaeth, M.; Barthlott, W. Superhydrophobicity of Biological and Technical Surfaces Under Moisture Condensation: Stability in Relation to Surface Structure. *Langmuir* **2008**, *24*, 13591–13597.

(21) Miljkovic, N.; Preston, D. J.; Enright, R.; Wang, E. N. Electric-Field-Enhanced Condensation on Superhydrophobic Nanostructured Surfaces. *ACS Nano* **2013**, *7*, 11043–11054.

(22) Miljkovic, N.; Wang, E. N. Condensation Heat Transfer on Superhydrophobic Surfaces. *MRS Bull.* **2013**, *38*, 397–406.

(23) Enright, R.; Miljkovic, N.; Alvarado, J. L.; Kim, K.; Rose, J. W. Dropwise Condensation on Micro- and Nanostructured Surfaces. *Nanoscale Microscale Thermophys. Eng.* **2014**, *18*, 223–250.

(24) Wisdom, K. M.; Watson, J. A.; Qu, X.; Liu, F.; Watson, G. S.; Chen, C.-H. Self-Cleaning of Superhydrophobic Surfaces by Self-Propelled Jumping Condensate. *Proc. Natl. Acad. Sci.* **2013**, *110*, 7992–7997.

(25) Boreyko, J. B.; Zhao, Y.; Chen, C. H. Planar Jumping-Drop Thermal Diodes. *Appl. Phys. Lett.* **2011**, *99*, 234105.

(26) Boreyko, J. B.; Chen, C.-H. Vapor Chambers with Jumping-Drop Liquid Return from Superhydrophobic Condensers. *Int. J. Heat Mass Transf.* **2013**, *61*, 409–418.

(27) Zhang, Q.; He, M.; Chen, J.; Wang, J.; Song, Y.; Jiang, L. Anti-Icing Surfaces Based on Enhanced Self-Propelled Jumping of Condensed Water Microdroplets. *Chem. Commun.* **2013**, *49*, 4516–4518.

(28) Chen, X.; Ma, R.; Zhou, H.; Zhou, X.; Che, L.; Yao, S.; Wang, Z. Activating the Microscale Edge Effect in a Hierarchical Surface for Frosting Suppression and Defrosting Promotion. *Sci. Rep.* **2013**, *3*, 2515, doi:10.1038/srep02515.

(29) Miljkovic, N.; Preston, D. J.; Enright, R.; Wang, E. N. Jumping-Droplet Electrostatic Energy Harvesting. *Appl. Phys. Lett.* **2014**, *105*, 013111.

(30) Khawaji, A. D.; Kutubkhanah, I. K.; Wie, J. M. Advances in Seawater Desalination Technologies. *Desalination* **2008**, *221*, 47–69.

(31) Foresti, D.; Nabavi, M.; Klingauf, M.; Ferrari, A.; Poulikakos, D. Acoustophoretic Contactless Transport and Handling of Matter in Air. *Proc. Natl. Acad. Sci.* **2013**, 12549–12554, doi: 10.1073/pnas.1301860110.

(32) Jaworek, A.; Krupa, A.; Sobczyk, A. T.; Marchewicz, A.; Szudyga, M.; Antes, T.; Balachandran, W.; Di Natale, F.; Carotenuto, C. Submicron Particles Removal by Charged Sprays. Fundamentals. *J. Electrost. Electrost. 2013 12th Int. Conf. Electrost.* **2013**, *71*, 345–350.

(33) Kollera, M.; Grigull, U. Über das Abspringen von Tropfen bei der Kondensation von Quecksilber. *Wärme - Stoffübertragung* **1969**, *2*, 31–35.

(34) Paulsen, J. D.; Burton, J. C.; Nagel, S. R.; Appathurai, S.; Harris, M. T.; Basaran, O. A. The Inexorable Resistance of Inertia Determines the Initial Regime of Drop Coalescence. *Proc. Natl. Acad. Sci.* **2012**, *109*, 6857–6861.

(35) Paulsen, J. D.; Burton, J. C.; Nagel, S. R. Viscous to Inertial Crossover in Liquid Drop Coalescence. *Phys. Rev. Lett.* **2011**, *106*, 114501.

(36) Duchemin, L.; Eggers, J.; Josserand, C. Inviscid Coalescence of Drops. *J. Fluid Mech.* **2003**, *487*, 167–178.

(37) Thoroddsen, S. T.; Takehara, K.; Etoh, T. G. The Coalescence Speed of a Pendent and Sessile Drop. *J. Fluid Mech.* **2005**, *527*, 85–114.

(38) Wu, M.; Cubaud, T.; Ho, C.-M. Scaling Law in Liquid Drop Coalescence Driven by Surface Tension. *Phys. Fluids* **2004**, *16*, L51–L54.

(39) Eggers, J.; Lister, J. R.; Stone, H. A. Coalescence of Liquid Drops. *J. Fluid Mech.* **1999**, *401*, 293–310.

(40) Sprittles, J. E.; Shikhmurzaev, Y. D. Coalescence of Liquid Drops: Different Models Versus Experiment. *Phys. Fluids* **2012**, *24*, 122105.

(41) Sprittles, J. E.; Shikhmurzaev, Y. D. Finite Element Simulation of Dynamic Wetting Flows as an Interface Formation Process. *J. Comput. Phys.* **2013**, *233*, 34–65.

(42) Boreyko, J. B.; Baker, C. H.; Poley, C. R.; Chen, C.-H. Wetting and Dewetting Transitions on Hierarchical Superhydrophobic Surfaces. *Langmuir* **2011**, *27*, 7502–7509.

(43) Liu, T. Q.; Sun, W.; Sun, X. Y.; Ai, H. R. Mechanism Study of Condensed Drops Jumping on Super-Hydrophobic Surfaces. *Colloids Surf. A* **2012**, *414*, 366 – 374.

(44) Hart, A. J.; Slocum, A. H. Rapid Growth and Flow-Mediated Nucleation of Millimeter-Scale Aligned Carbon Nanotube Structures from a Thin-Film Catalyst. *J. Phys. Chem. B* **2006**, *110*, 8250–8257.

(45) Nam, Y.; Sungtaek, Y. A Comparitive Study of the Morphology and Wetting Characteristics of Micro/Nanostructured Cu Surfaces for Phase Change Heat Transfer Applications. *J Adhes. Sci. Technol.* **2013**, *27*, 2163–2176.

(46) Shikhmurzaev, Y. D. *Capillary Flows with Forming Interfaces*; CRC Press, 2007.

(47) Sprittles, J. E.; Shikhmurzaev, Y. D. Finite Element Framework for Describing Dynamic Wetting Phenomena. *Int. J. Numer. Methods Fluids* **2012**, *68*, 1257–1298.

Figure and table legends

Figure 1 - Hydrophobic CNT turf. (a) SEM image of CNT surface with P2i hydrophobic coating. (b) AFM scan in soft-tapping mode of the P2i-coated CNT surface. The scan revealed a maximum height variation of ~820 nm consistent with the height measured from SEM images. (c) Macroscopic droplet in the receding state on the P2i-coated CNT surface ($\theta_{app}^r = 166° \pm 2°$). (d) ESEM image of condensed droplets taken at an inclination angle of 8° from the horizontal plane. (e) Advancing contact angles on the P2i-coated CNT turf measured from the ESEM images (open circles). The solid curve is defined by $\theta_{app} = \cos^{-1}(r_p/R) + 90°$ with a conservatively estimated pinned base radius under the droplet of $r_p = 100$ nm. The horizontal dashed line represents the macroscopically measured advancing apparent contact angle, $\theta_a^{app} = 170.2° \pm 2.4°$.

Figure 2 - Jumping droplet trajectory. (a) High-speed time-lapse images capturing coalescence-induced droplet jumping ($T_w = 5$ °C, $p_v = 0.87$ kPa). Shutter speed: 185 µs. Scale bar: 100 µm. Inset: Overhead view of droplets prior to jumping where $R_1 = 20.2$ µm (left) and $R_2 = 19$ µm (right) ($R_j = 24.7$ µm). Scale bar: 20 µm. (b) Droplet velocity as a function of height above the surface. The line shows the fitted trajectory given by Eq. S1, indicating a jumping velocity of $v_j = 0.41 \pm 0.01$ m/s. Inset: Root mean square error (RMSE) of the fit of Eq. S1 to the measured velocities. The estimated jumping velocity was evaluated at the minima of the calculated RMSE. (c) Jumping velocity in (b) scaled by the characteristic speed given by Eq. (1), indicating $v_j/U = 0.21 \pm 0.01$.

Figure 3 – Internal flow field during droplet coalescence. (a) Schematic of two condensed droplets undergoing coalescence defined by an initial radius R, a time-varying capillary bridge radius r_b and a time-varying capillary bridge width $w = r_b^2/R$ on a superhydrophobic surface characterized by $\theta_a^{app} \rightarrow 180°$. A cylindrical coordinate system (r, z, β) is defined with the origin at the point where the two droplets meet. The z-coordinate is parallel to the surface, while the radial r-coordinate is resolved into y- and x-coordinates at $\beta = \pi/2$ (pointed to the top of the page) and $\beta = 0$ (pointed into the page), respectively. (b-f) Numerically simulated flow field of the coalescence process for $Oh = 0.012$ ($R = 100$ µm) and $1/4 < r_b/R \leq 2^{1/3}$ in the region of the droplet indicated by the dot-dashed box in (a). Simulated fluid properties: $\gamma = 72x10^{-3}$ N/m, $\rho = 1x10^3$ kg/m³, $\mu = 1x10^{-3}$ Pa.s. The contours depict the radial velocity component with red and blue coloring indicating flow away and towards the z-axis, respectively. The grey lines depict the streamlines of the flow. At the earlier stage of coalescence (b), the generated radial flow is restricted primarily to the local bridge region ($z/R = 0$). This flow is fed by a region of negative radial flow that can be clearly seen in (c) due to the differences in the local curvature along the droplet interface. In (d), the positive and negative radial flow regions expand as the capillary wave moves away from the bridge region. In (e), the negative radial flow feeding the positive radial flow centered around $z/R = 0$ has arrived at the edge of the droplet. (f) The negative radial flow has vanished and the entire upper portion of the droplet has a positive radial velocity driven by the curvature difference between the interface at $z/R \approx 1.75$ ($r/R \approx 0$) and $z/R \approx 0$ ($r/R \approx 2^{1/3}$).

Figure 4 – Capillary wave during droplet coalescence. Pressure profiles at the liquid/vapor interface along the normalized interface position, $s(r,z)/R$. The pressure difference across the interface is normalized by the initial equilibrium pressure of the two droplets, $\Delta p(R) = 2\gamma/R$. The light horizontal solid line and dashed line correspond to $\Delta p/\Delta p(R) = 1$ and $\Delta p(2^{1/3}R)/\Delta p(R) \approx 0.8$, respectively. The solid curve (black) depicts the pressure profiles obtained for $Oh = 0.012$ corresponding to the flow fields shown in Figure 3. The dashed (green) and dash-dot (red) curves depict the pressure profiles obtained for $Oh = 0.037$ and $Oh = 0.118$, respectively.

Figure 5 - Viscous dissipation & momentum generation. (a) Viscously dissipated energy scaled by the excess surface energy budget during the coalescence process up to $r_b/R = 2^{1/3}$ for $Oh = 0.012$ (solid

curve), $Oh = 0.037$ (dashed curve) and $Oh = 0.118$ μm (dot-dashed curve). (b) Viscously dissipated energy at $r_b/R = 2^{1/3}$ (circles) scaled by the excess surface energy budget as a function of the Oh number. The dashed and dot-dashed lines correspond to the viscous dissipation terms estimated in ref. [13] and [9], respectively. (c) Numerically simulated positive and negative momentum y-components ($y > 0$) scaled by the characteristic momentum as a function of the bridge radius for $Oh = 0.012$ (solid curve), $Oh = 0.037$ (dashed curve) and $Oh = 0.118$ μm (dot-dashed curve). The dashed line corresponds to Eq. (5) with $C = 1.3$. The vertical solid line corresponds to $r_b/R = 2^{1/3}$. The simple inertial model of the bridging phase (dot curve) shows good agreement with the low Oh number data up to $r_b/R \approx 1$. For increasing Oh number, we observe a deviation from the simple inertial model. (d) Maximum value of the dimensionless y-component momentum in the upper portion of the droplets $p_y^+\big|_{\max(r_b/R \geq 2^{1/3})}/(m_j U)$ contributing to the droplet jumping velocity as a function of Oh number (squares). Sum of the dimensionless y-component momentum contributions $\Sigma p_y/(m_j U)$ to the droplet jumping velocity given by Eq. (6) as a function of Oh number (circles). Both the y-component momentum in the upper portion of the droplets and the total momentum scale approximately as $\sim -Oh$.

Figure 6 – Comparison of experimental data to numerical predictions. Jumping velocities as a function of jumping droplet diameter for (a) the two-camera arrangement and (b) the one-camera arrangement with properties evaluated at (a) $T_w = 278$ K and (b) $T_w = 299$ K to correspond with the experimental conditions. The dimensionless jumping velocity is plotted as a function of Oh in (c). In (a), the open circles are the data from the two-camera arrangement for the P2i-CNT surface and the open triangles are the data from ref. [7]. In (b), the squares and diamonds are the data from the one-camera arrangement for the P2i-CNT and P2i-CuO surfaces, respectively. In (a-c), the closed circles show the prediction of the numerical simulations (Figure 5d) and the solid line is given by Eq. (7). The dot-dashed lines in (a-c) represent the bounds of $p_y^+\big|_{\max(r_b/R \geq 2^{1/3})}$ and $2p_y^+\big|_{\max(r_b/R \geq 2^{1/3})}$.
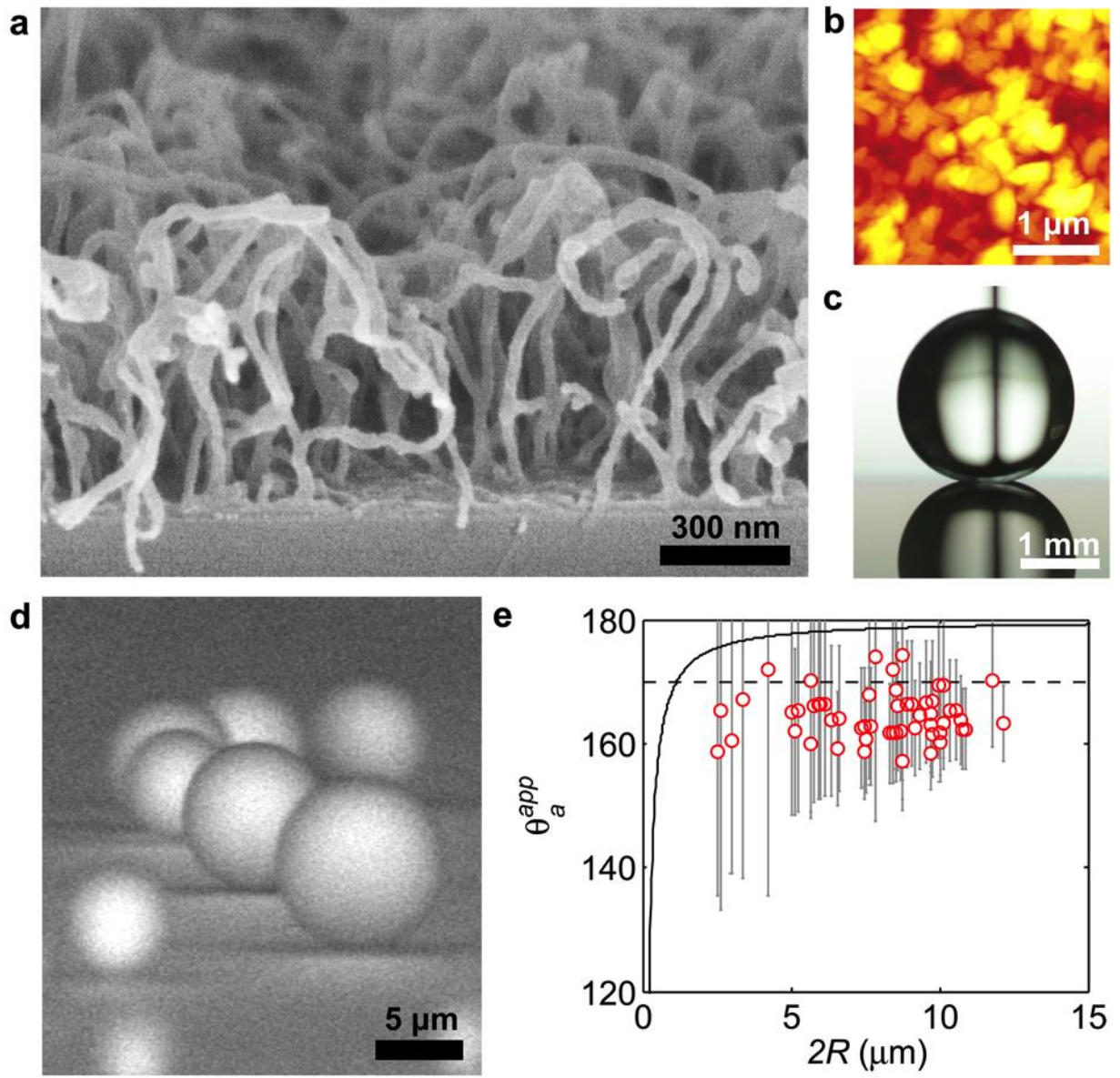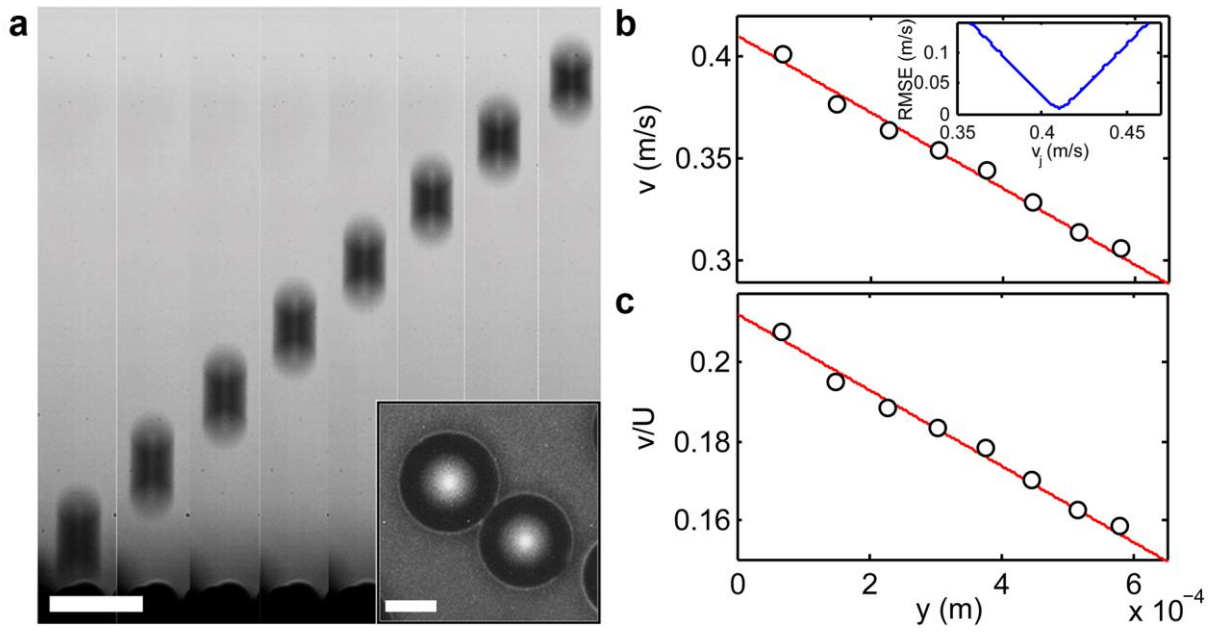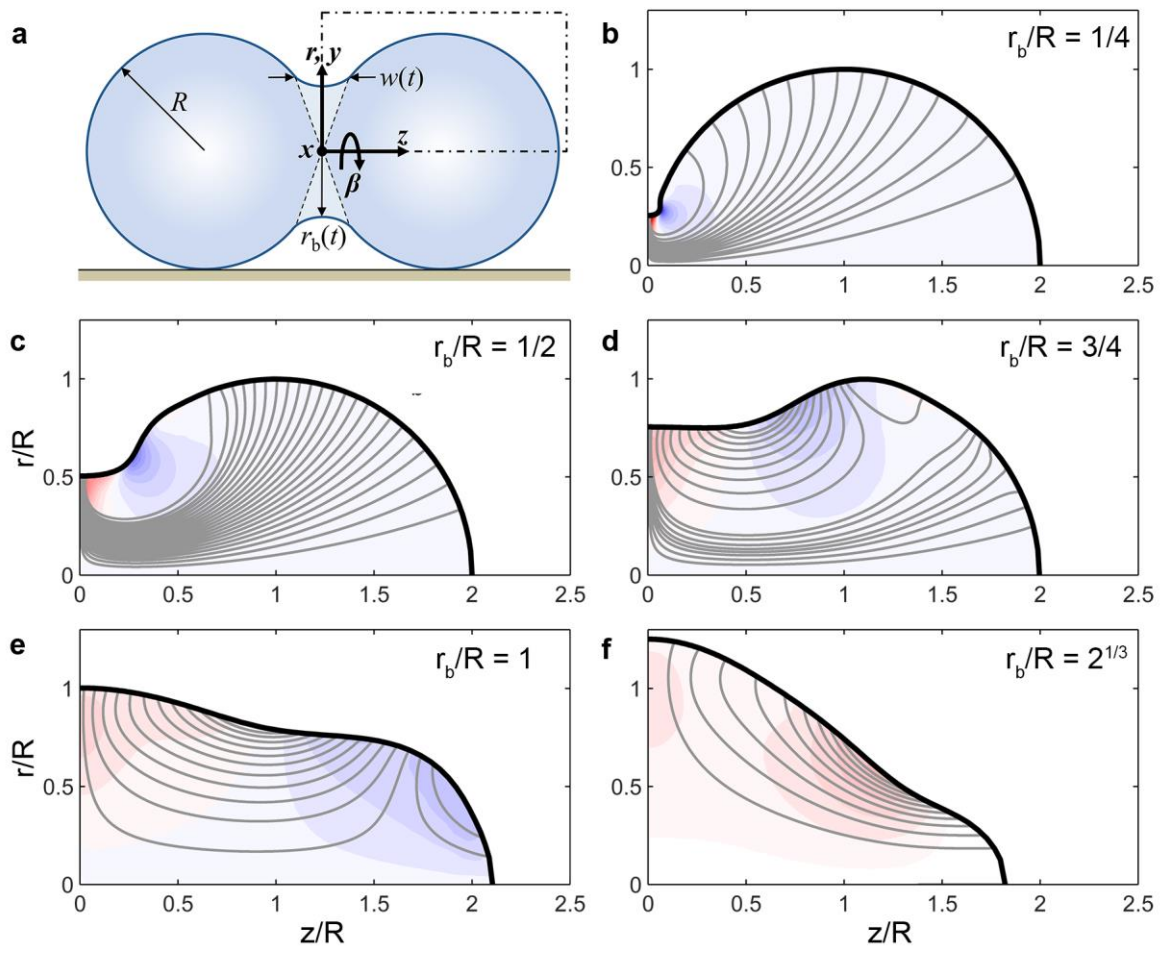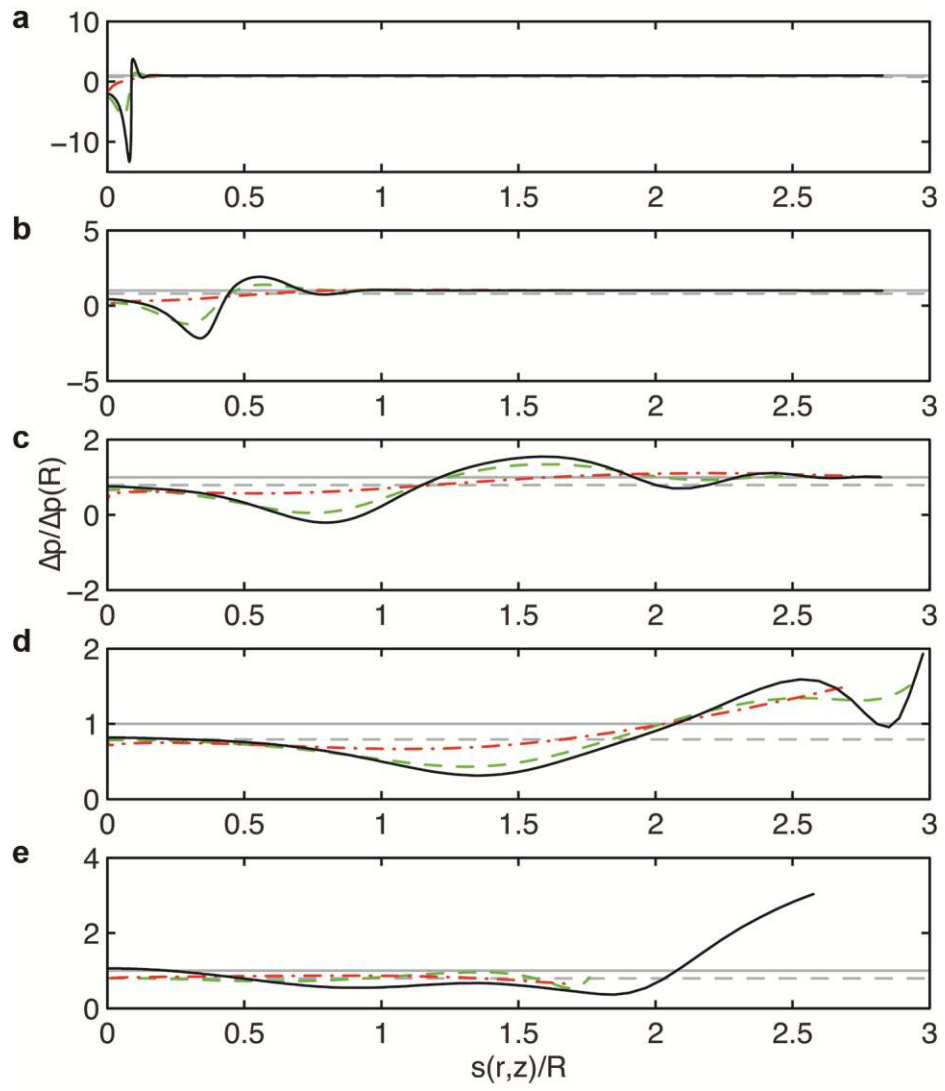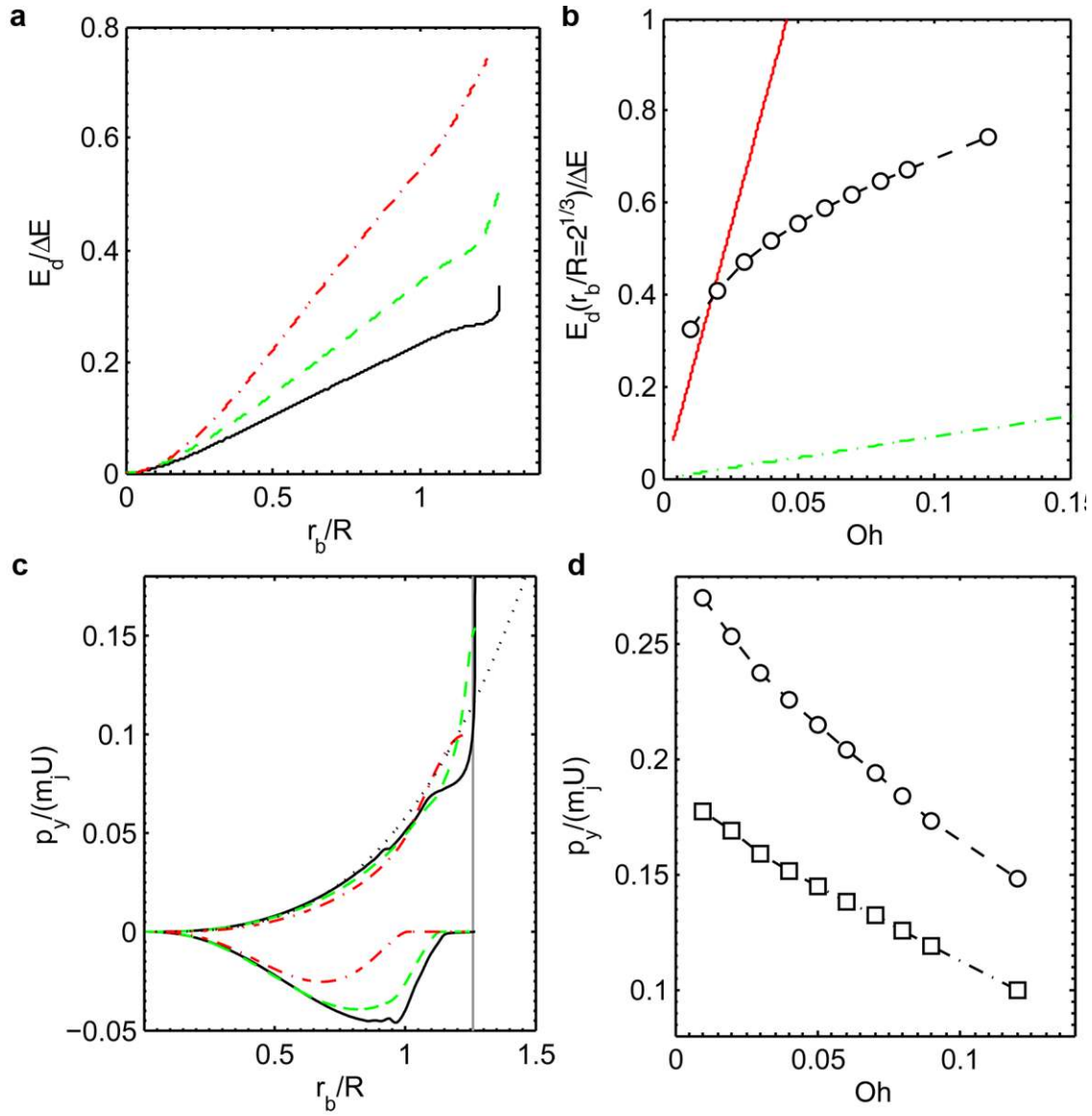
Figure 1

Figure 2

Figure 3

Figure 4

Figure 5

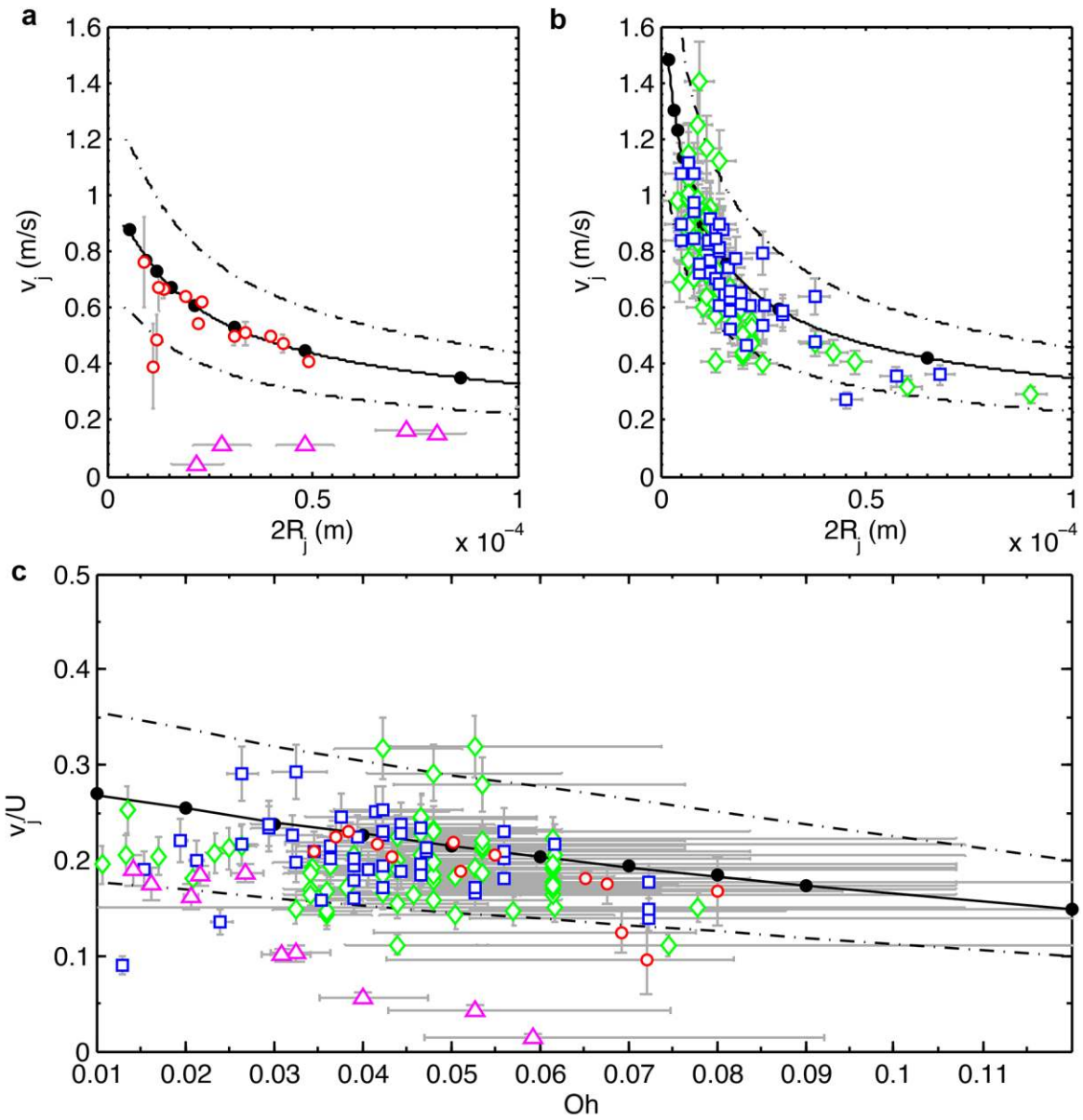Figure 6

Supporting Information

How Coalescing Droplets Jump

Ryan Enright[1,§,*], Nenad, Miljkovic[2,3], James Sprittles[4], Kevin Nolan[1], Robert Mitchell[5,†] and Evelyn N. Wang[2,*]

[1]*Thermal Management Research Group, Efficient Energy Transfer (ηET) Dept., Bell Labs Ireland, Alcatel-Lucent Ireland Ltd., Blanchardstown Business & Technology Park, Snugborough Rd. Dublin 15, Ireland*
[2]*Department of Mechanical Engineering, Massachusetts Institute of Technology, 77 Massachusetts Avenue, Cambridge, Massachusetts, 02139, USA*
[3]*Department of Mechanical Science and Engineering, University of Illinois, Urbana, Illinois, 61801, USA*
[4]*Mathematics Institute, University of Warwick, Coventry, CV4 7AL, UK*
[5]*Department of Materials Science and Engineering, Massachusetts Institute of Technology, 77 Massachusetts Avenue, Cambridge, Massachusetts, 02139, USA*
[§]Work initiated while affiliated with [2] and *Stokes Institute, University of Limerick, Ireland*
[†]Current address: *Intel Corp., 5200 NE Elam Young Parkway, m/s RA3-301, Hillsboro, Oregon 97124, USA.*

*Address correspondence to ryan.enright@alcatel-lucent.com and enwang@mit.edu

S1. HIGH SPEED MOVIE

Movie 1. Incoming droplet-triggered ejection captured with a high speed camera (Phantom v7.1, Vision Research). The P2i-coated CNT sample is oriented in the horizontal direction and mounted on a cold stage. The video was captured at 3,300 fps and is played back at 28.6 fps. The field of view is 200 μm x 350 μm.

S2. TWO-CAMERA JUMPING DROPLET EXPERIMENT SETUP
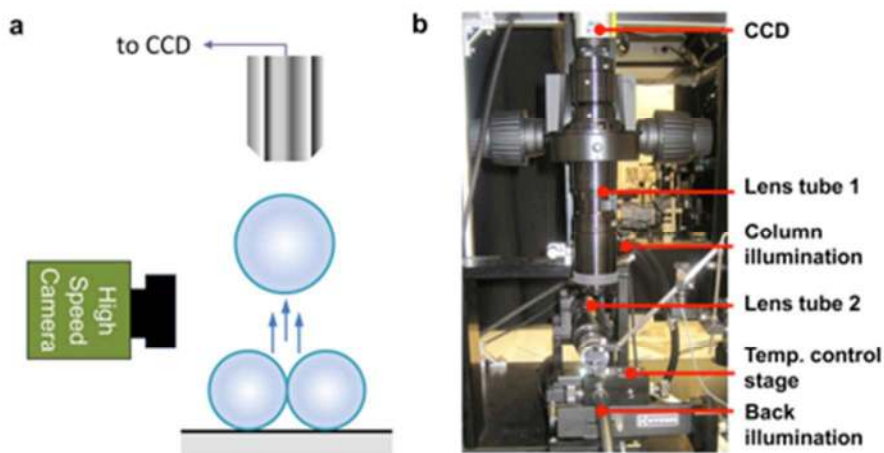
Figure S1 - Two-camera arrangement for measuring jumping droplet trajectories. a) Schematic of the measurement principle where a CCD camera captured the initial conditions prior to droplet coalescence and a high speed camera that captured the jumping droplet trajectory. Both cameras were focused at the same spatial position. The sample sat on a temperature controlled stage. b) Image of the experimental set-up (Kyowa Interface Science Ltd., MCA-3) showing the arrangement of the two cameras connected to lens tubes. The high-speed camera (not visible) was connected to lens tube 2.
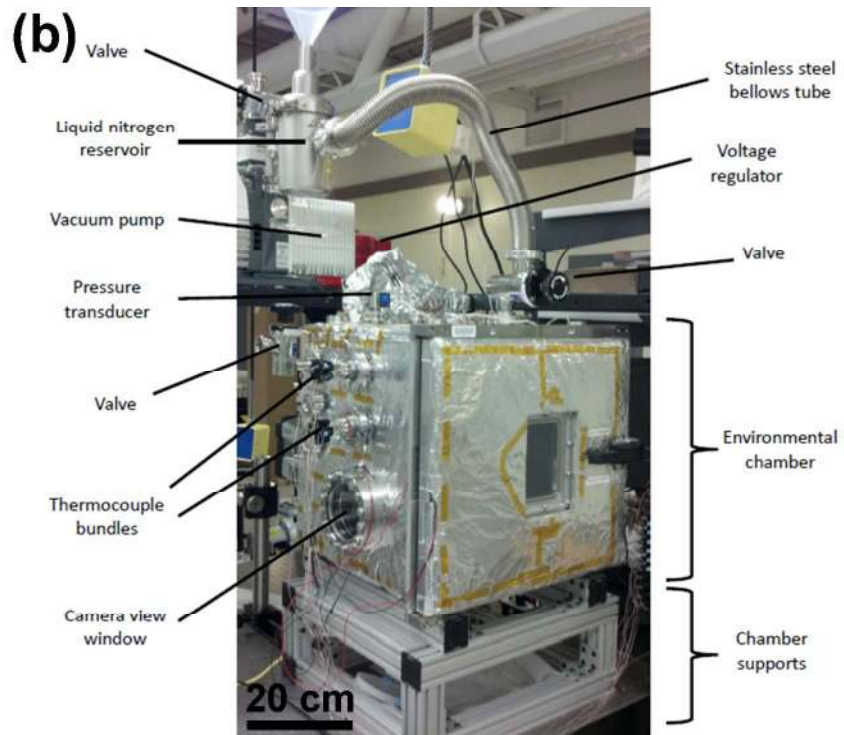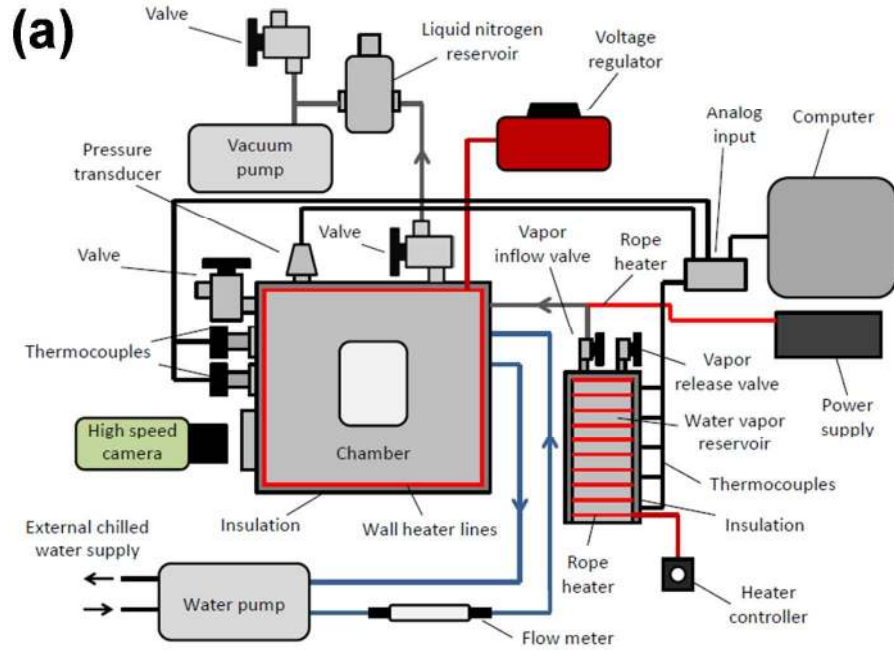
S3. CONDENSATION CHAMBER SETUP

The custom environmental chamber used for this work (Kurt J. Lesker) consists of a stainless steel frame with a door (sealed with a rubber gasket), two viewing windows, and apertures for various components. Resistive heater lines were wrapped around the exterior of the chamber walls to prevent condensation at the inside walls and then insulated on the exterior walls. The output power of the resistive heater lines was controlled by a voltage regulator (Variac). Two insulated stainless steel water flow lines (Swagelok) were fed into the chamber *via* a KF flange port (Kurt J. Lesker) to supply cooling water to the chamber from a large capacity chiller (System III, Neslab).
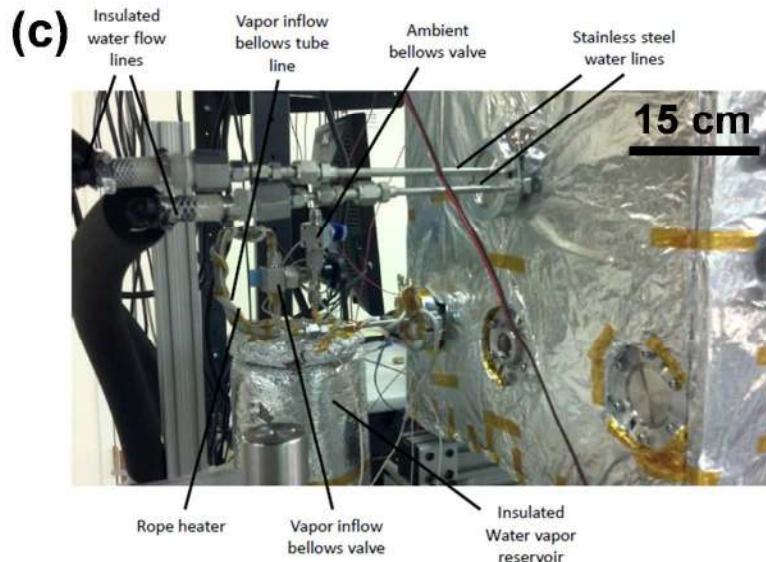
A secondary stainless steel tube line was fed into the chamber *via* a KF adapter port that served as the flow line for the incoming water vapor supplied from a heated steel water reservoir. The vapor line was wrapped with a rope heater (60 W, Omega) and controlled by a power supply (Agilent). The vapor reservoir was wrapped with another independently-controlled rope heater (120 W, Omega) and insulated to limit heat losses to the environment. The access tubes were welded to the vapor reservoir, each with independently-controlled valves. The first valve (Diaphragm Type, Swagelok), connecting the bottom of the reservoir to the ambient, was used to fill the reservoir with water. The second valve (BK-60,

Swagelok), connecting the top of the reservoir to the inside of the chamber, provided a path for vapor inflow. K-type thermocouples were located along the length of the water vapor reservoir to monitor temperature.

A bellows valve (Kurt J. Lesker) was attached to the chamber to serve as a leak port between the ambient and inside of the chamber. In order to monitor temperatures within the chamber, K-type thermocouple bundles were connected through the chamber apertures *via* a thermocouple feed through (Kurt J. Lesker). To provide electrical connections inside the chamber for LED lighting and electric field generation, insulated copper electrical wires were connected through the chamber apertures *via* an electrical feed through (Kurt J. Lesker). A pressure transducer (925 Micro Pirani, MKS) was attached to monitor pressure within the chamber. The thermocouple bundles and the pressure transducer were both electrically connected to an analog input source (RAQ DAQ, National Instruments), which was interfaced to a computer for data recording. A second bellows valve (Kurt J. Lesker) was integrated onto the chamber for the vacuum pump, which brought down the chamber to vacuum conditions prior to vapor filling. A liquid nitrogen cold trap was incorporated along the line from the chamber to the vacuum which served to remove any moisture from the pump-down process and ultimately assist in yielding higher quality vacuum conditions. A tertiary bellows valve (Kurt J. Lesker) was integrated on a T fitting between the vacuum pump and liquid nitrogen reservoir to connect the vacuum line to the ambient to release the vacuum line to ambient conditions once pump down was achieved. In order to visually record data, a high speed camera (Phantom v7.1, Vision Research) was placed in line with the 5" viewing windows on the chamber. In addition, a digital SLR camera (Cannon) was interchangeable with the high speed camera to obtain color images. The schematic of the exterior of the environmental setup is depicted in **Figure S2**a. Images of the front and rear of the experimental setup are shown in **Figure S2**b and c, respectively.

(a)

Valve

Liquid nitrogen reservoir

Voltage regulator

Analog input

Computer

Vacuum pump

Pressure transducer

Valve

Valve

Vapor inflow valve

Rope heater

Vapor release valve

Thermocouples

High speed camera

Chamber

Water vapor reservoir

Thermocouples

Power supply

External chilled water supply

Insulation

Wall heater lines

Insulation

Rope heater

Heater controller

Water pump

Flow meter

(b)

Valve

Liquid nitrogen reservoir

Vacuum pump

Pressure transducer

Valve

Thermocouple bundles

Camera view window

Stainless steel bellows tube

Voltage regulator

Valve

Environmental chamber

Chamber supports

20 cm

Figure S2 – (a) Schematic of experimental setup (not to scale). (b) Image of the experimental setup shown from the front (high speed camera and data acquisition system not shown). (c) Image of the experimental setup from the rear of the chamber showing the cooling water inlet and outlet and water vapor reservoir.

S4. SINGLE CAMERA CONDENSATION PROCEDURE

For each experimental trial, a set of strict procedures were followed to ensure consistency throughout the experiments. The first step of the process was to turn on the voltage regulator to heat up the environmental chamber walls, which prevented condensation on the chamber walls. Simultaneously, the water vapor reservoir was filled with approximately 3.5 liters of DI water (99% full) using a syringe through the vapor release valve. After opening the vapor inflow valve and closing the vapor release valve, the rope heater around the water vapor reservoir was turned on with the heater controller set to maximum output (120 W). Then the rope heater connected to the vapor inflow valve was turned on. The temperature of the water reservoir was monitored with the installed thermocouples; the temperature at the top of the reservoir was higher than that of the middle/bottom of the reservoir due to the water thermal-mass present at the middle/bottom section. Hence, we ensured that the regions of the water reservoir of higher thermal capacity were brought to a sufficiently high temperature for boiling. During the boiling process, aluminum foil was placed on the bottom surface of the inner chamber to collect any of the water leaving the vapor inflow line. Once boiling was achieved and all thermocouples on the reservoir were > 95°C for at least 10 minutes, the vapor inflow valve was closed. The excess water that spilled inside the chamber during de-gassing of the reservoir was removed.

In order to install the samples onto the rig (**Figure S3**), the Swagelok female adapters at the ends of the tube samples were connected to the 90 degree male elbow connecters on the rig. Before installing the

entire sample setup in the chamber, all adapters/connecters were tightened to ensure that there were no leaks that could affect vacuum performance. The setup was then placed on top of the steel supports and the bellows tubes (for the water inflow/outflow) were connected to the water lines. Then the insulating wet bulb wick was placed near the sample and in contact with the bottom surface of the chamber.

The next step was to begin the vacuum pump-down procedure. Initially, the liquid nitrogen cold trap was filled to about half capacity. The ambient exposed valves connecting the chamber and the vacuum pump were both closed and the valve connected to the liquid nitrogen cold trap was opened. The vacuum pump was then turned on, initiating the pump-down process. The pressure inside the chamber was monitored during the pump-down process. This process took approximately one hour in order to achieve the target vacuum conditions (0.5 Pa < P < 1 Pa). The experimental operating pressure of non-condensable was set to be a maximum of 0.25% of the operating pressure. Non-condensable gas content of above 0.5% (pressure) was shown to significantly degrade performance during dropwise condensation. In our experiments, extreme care was taken to properly de-gas the vacuum chamber and water vapor reservoir prior to experimental testing. In addition, the chamber leak rate was characterized prior to each run in order to estimate the maximum time available for acquiring high fidelity data with non-condensable content of less than 0.25%.

The setup of the water flow-loop is described as follows. The Neslab water pump reservoir was filled and turned on to a flow rate of 5 L/min ($0 < \Delta T_{LMTD} < 15$ K). The flow rate was monitored with the flow meter integrated in the inflow water line. In order to bring the chilled water into the flow loop and to the tube sample, the external chilled water lines were opened.

Prior to beginning experiments, the high-speed camera was turned on for visual recording of the sample during condensation. Afterwards, the rope heater around the water reservoir was turned off and the vapor inflow valve was slowly turned open until the operating pressure was reached. Steady state conditions were typically reached after 2 minutes of full operation.

The droplet ejection process was captured under saturated conditions inside the environmental chamber using a single-camera setup[3]. The out-of-plane trajectory of the ejected droplets was captured using a high-speed camera (Phantom v7.1, Vision Research) at frame capture rates of 7200, 10000 and 20000 Hz corresponding to shutter speeds of 139 μs, 100 μs and 50 μs, respectively. The camera was mounted outside the environmental chamber and fitted with an extended macro lens assembly (**Figure S3**a). The lens assembly consisted of a fully extended 5X optical zoom macro lens (MP-E 65 mm, Canon),

connected in series with 3 separate 68 mm extension tubes (Auto Extension Tube Set DG, Kenko). The DG extension tubes enable the lens to focus closer than its normal set minimum focal distance, which has the effect of magnifying the image (making it appear larger in the viewfinder). The DG extension tubes have no optics. They were mounted in between the camera body and lens to create more distance between the lens and film plane. By moving the lens further away from the film or CCD sensor in the camera, the lens was allowed to focus much closer than normal. Illumination was supplied by light emitting diodes installed inside the chamber and providing back lighting to the sample.

The experiment was initiated by first evacuating the environmental chamber to medium-vacuum levels ($=0.5 \pm 0.025$ Pa). The sample was mounted to a flattened copper tube connected to an external cooling loop and was maintained at a temperature of $T_w = 26$ °C ($p_w = 3.33$ kPa) (Figure S3b,c). The water vapor supply was vigorously boiled before the experiments to remove non-condensable gases. Water vapor was introduced into the environmental chamber *via* a metering valve set to maintain the chamber pressure at $p_v = 3.6 \pm 0.175$ kPa. Figure S4 shows a typical high speed time-lapse obtained during jumping-droplet condensation.
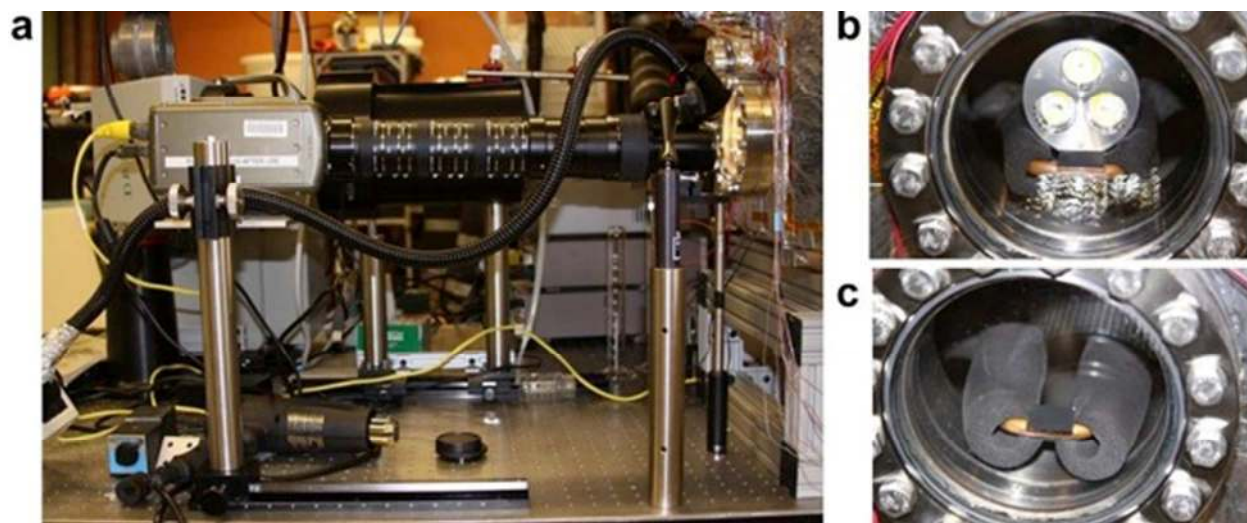
Figure S3 - High speed and high magnification imaging setup for jumping droplets. Images of the (a) experimental setup showing the high speed camera placed adjacent to the chamber and retrofitted with extension tubes for higher magnification imaging. Images showing the sample holder inside the chamber (b) with LED light placed behind and (c) without LED light.
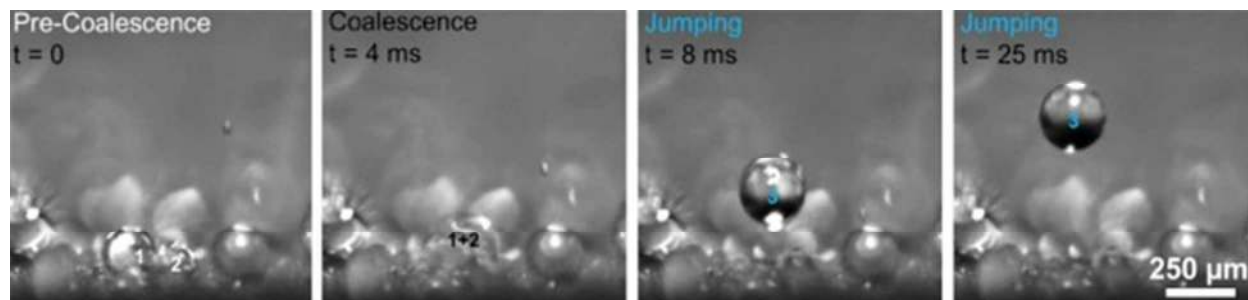
Figure S4 - High speed droplet jumping images. Time-lapse images captured *via* high speed camera (**Figure S3**) of water condensation on the nanostructured CuO surface. Droplet 1 and 2 initially grow independently until coalescing and then jumping from the surface (P_v = 3600 ± 175 Pa, T_s = 26 ± 0.2˚C).

S5. MEASURING JUMPING VELOCITY FROM FITTED DROPLET TRAJECTORY & ESTIMATING ENTRAINING VAPOR FLOW FOR AMBIENT EXPERIMENT

The general form of the vertical jumping droplet trajectory can be found by considering the following force balance

$$m_j \frac{dv}{dt} = -m_j g - \frac{1}{2} \rho \pi R_j^2 (v - v_f)^2 C_d,$$

Eq. S1

where R_j, $m_j = \rho(4/3)\pi R_j^3$ and g are the jumping droplet radius, jumping droplet mass and the gravitational constant ($g = 9.81$ m/s^2), respectively. The inertial force on the left-hand side of Eq. S1 is balanced by the gravitational force and a drag force characterized by a drag coefficient C_d that dissipates the kinetic energy of the jumping droplet traveling at a velocity $v(y)$. The drag term on the right-hand side of Eq. S1 also accounts for an entraining vapor flow with a velocity v_f associated with vapor moving towards the condensing surface to satisfy mass conservation [1,2]. The magnitude of this entrainment flow velocity for the two-camera arrangement at ambient conditions was estimated from experimentally observed droplet growth rates and found to be negligible for the range of condensation conditions explored here, *i.e.*, $|v_f| = 1.2 x 10^{-3}$ m/s $\ll |v|$, (see **Figure S5**). For the one-camera arrangement in the environmental chamber, the heat flux could be directly measured and was found to be $q'' < 0.1$ W/cm^2 for all measurements, corresponding to $|v_f| = q''/(\rho_v h_{fg}) < 0.016$ m/s; at least an order of magnitude smaller than typical jumping droplet speeds. Thus, v_f was approximated as zero in Eq. S1. A possible additional drag force due to viscous interactions in the gap opening up between the departing droplet and the surface discussed in ref. [3] was neglected due to the large Knudsen number expected in the gap between the departing droplet and the condensing surface. Electrostatic effects due to the charged nature of the jumping droplets on the force balance were also neglected on the basis that no external electric fields were imposed on the system [4].

Using the characteristic speed given by Eq. **1**, the Reynolds (*Re*) number under ambient conditions (two-camera arrangement) was calculated to be as large as 10 over the range of experimental droplet diameters

$(10 \lesssim 2R_{\mathrm{j}} < 200$ μm), indicating the possibility of a non-linear drag regime, $Re = \rho_g U 2R_j / \mu_g \lesssim 10$, where ρ_g and μ_g are the density and dynamic viscosity of the surrounding gas, respectively. Thus, the drag coefficient in Eq. S1 was calculated from an expression accounting for a Re-dependent drag coefficient given by [5],

$$C_D = \frac{8}{Re}\frac{3\lambda + 2}{\lambda + 1}\left(1 + 0.05\frac{3\lambda + 2}{\lambda + 1}Re\right) - 0.01\frac{3\lambda + 2}{\lambda + 1}Re\ln(Re), \qquad \text{Eq. S2}$$

where $\lambda = \mu / \mu_g$ is the dynamic viscosity ratio between the liquid and gas phases, under the assumption of a spherical droplet shape during flight. For $R_{\mathrm{j}} \sim 10$ μm, a liquid density $\rho \approx 1000$ kg/m^3, a gas density range $\rho_{\mathrm{g}} \approx 0.02 - 1.2$ kg/m^3, a gas dynamic viscosity $\mu_{\mathrm{g}} \approx 9.8$ μPa·s and $\gamma \approx 72$ mN/m, this assumption is justified given that the Bond number $Bo = \left(\rho g R_j^2\right)/\gamma \ll 1$, Weber number $We = \left(\rho_g U^2 R_j\right)/\gamma \ll 1$, and Capillary number $Ca = \left(\mu_g U\right)/\gamma \ll 1$, suggesting minimal deformation of the water droplet by gravitational, inertial and viscous forces with respect to the surrounding gas [6]. Eq. S1 was solved numerically using an explicit Runge-Kutta method with a variable time step. The initial jumping droplet velocity, $v_j = v(y = 0)$, was then found by fitting the calculated result to the measured droplet trajectory.
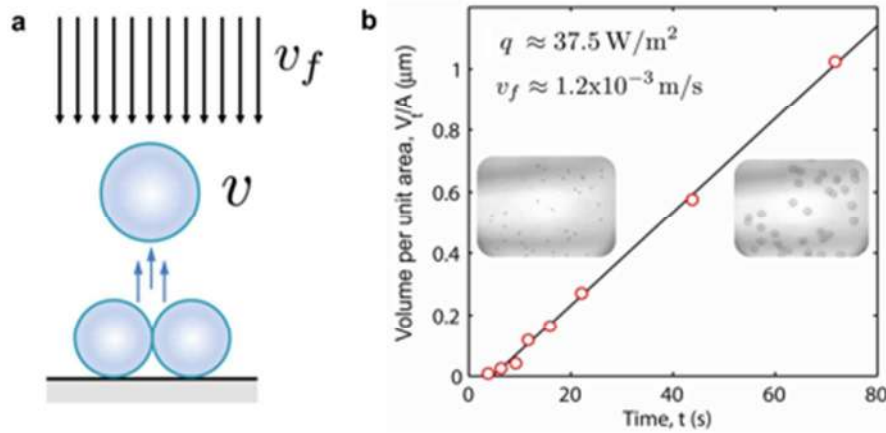
Figure S5 - Droplet entrainment due to vapor flow. a) Diagram of ejected droplet with velocity v moving through a uniform vapor flow with velocity $-v_{\mathrm{f}}$. b) Volume of condensed liquid on the surface per unit area as a function of condensation time before the onset of droplet coalescence. The slope of a linear fit to the data was used to estimate v_{f}.
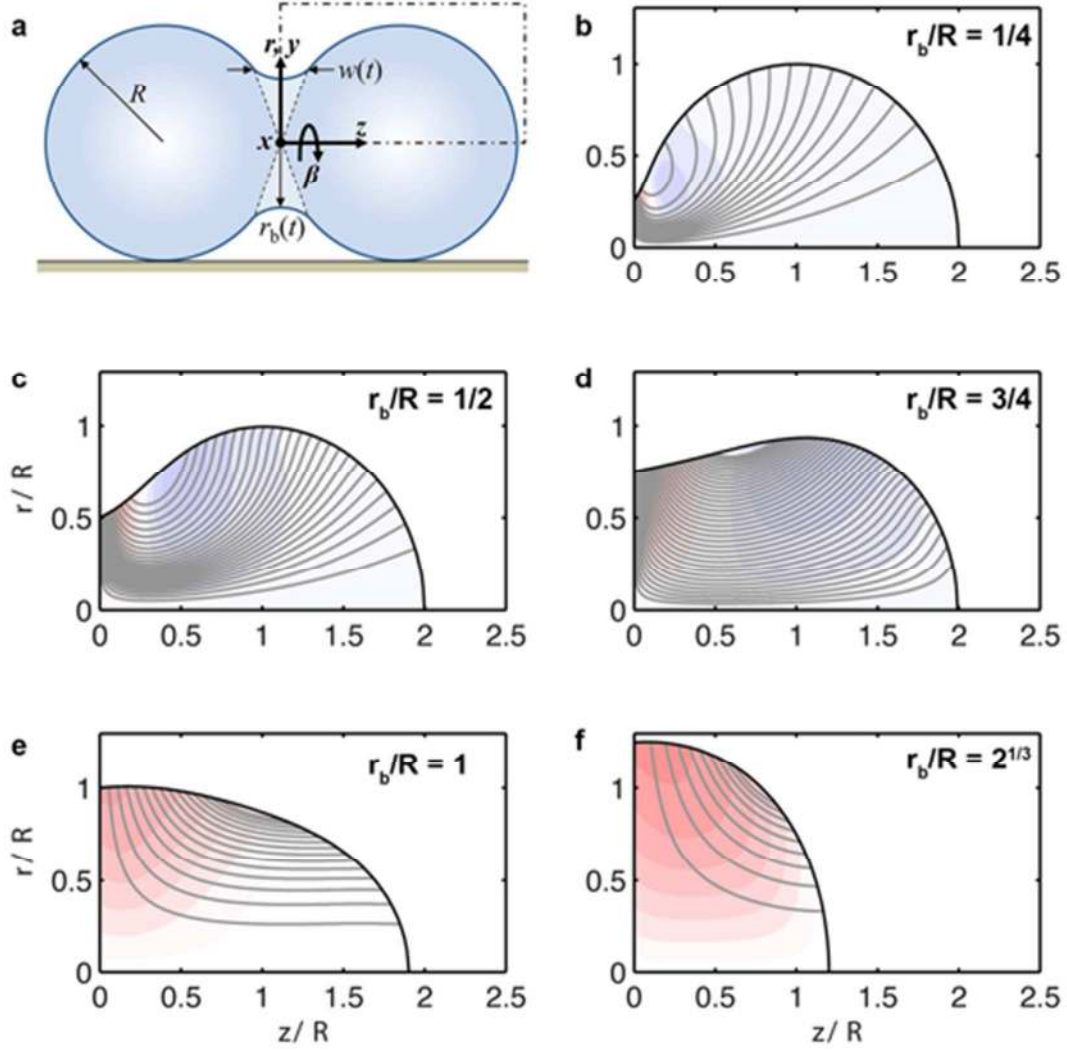
S6. FLOW FIELDS FOR LARGER *Oh* NUMBERS
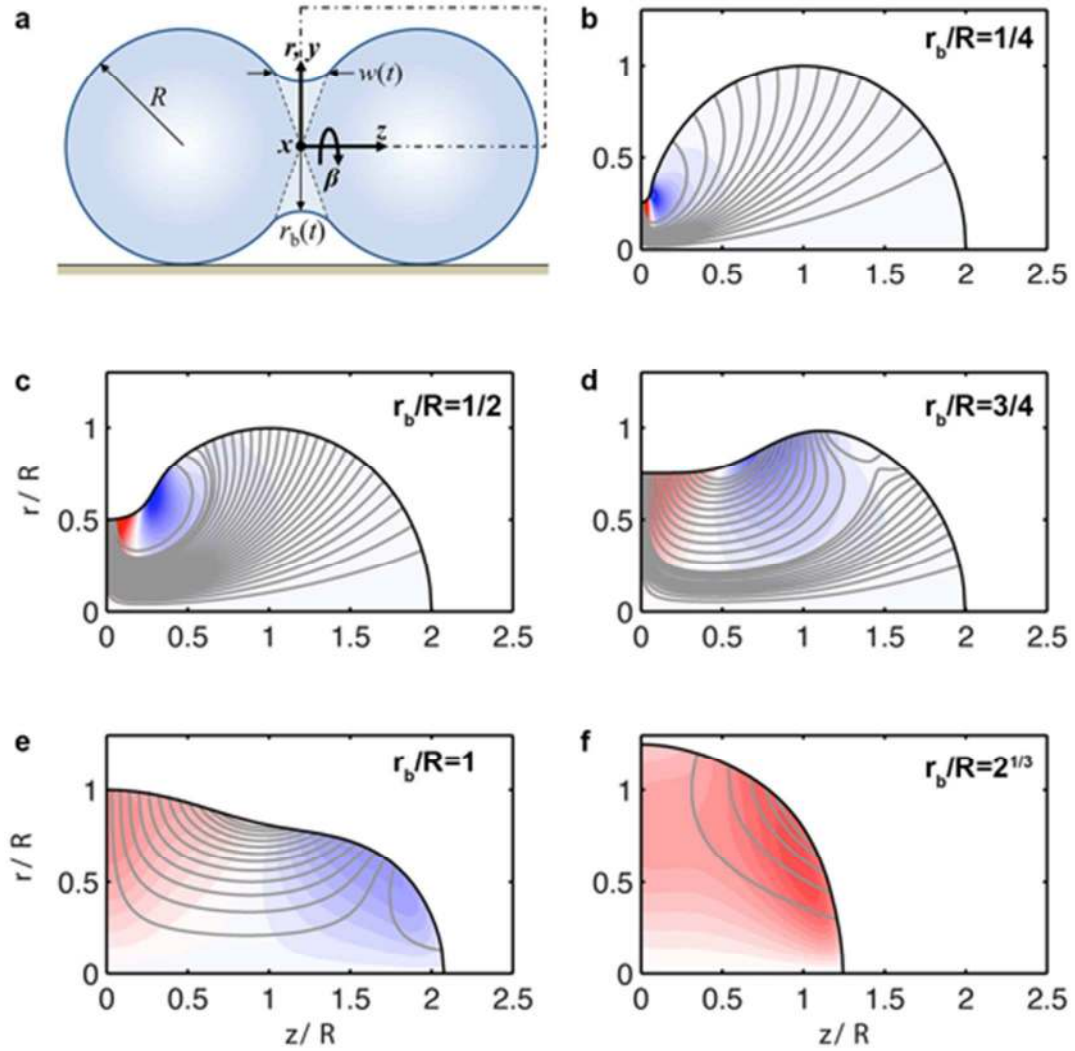
Figure S6 (color online) (b-f) Numerically simulated flow field of the coalescence process for $R = 10$ μm ($Oh = 0.037$) and $1/4 < r_b/R \leq 2^{1/3}$ in the region of the droplet indicated by the dot-dashed box in Fig 3a of the main manuscript. Simulation properties: $\gamma = 72x10^{-3}$ N/m, $\rho = 1x10^3$ kg/m^3, $\mu = 1x10^{-3}$ Pa.s. The contours depict the radial velocity component with red and blue coloring indicating flow away and towards the z-axis, respectively. The grey lines depict the streamlines of the flow.

Figure S7 (color online) (b-f) Numerically simulated flow field of the coalescence process for $R = 1$ μm ($Oh = 0.118$) and $1/4 < r_b/R \leq 2^{1/3}$ in the region of the droplet indicated by the dot-dashed box in Fig 3a of the main manuscript. Simulation properties: $\gamma = 72x10^{-3}$ N/m, $\rho = 1x10^3$ kg/m^3, $\mu = 1x10^{-3}$ Pa.s. The contours depict the radial velocity component with red and blue coloring indicating flow away and towards the z-axis, respectively. The grey lines depict the streamlines of the flow.

S7. ESTIMATING p_y^+ OF THE BRIDGING FLOW

To develop a model description of the momentum developed by the bridge flow ($r_b/R < 1$), we consider the following. As the bridge develops, the flow moving perpendicular to the bridge, *i.e.*, fed by the negative radial flow near the bridge front, expands the radial flow region behind the bridge front such that the width of the radial bridging flow varies from a maximum at the bridge front ($r = r_b$) to approximately zero at $r = 0$. A simple estimate of the volume of the induced radial flow can be given by defining a linearly varying width

$$x(r) = \frac{r}{r_b}w,$$

<div align="right">Eq. S3</div>

where, from geometric considerations valid for small r_b/R, the width of the bridge front at $r = r_b$ is $w = r_b^2/R$ [7,8]. Furthermore, we approximate the radial velocity as decreasing linearly from a maximum of v_b at $r = r_b$ to zero at $r_b = 0$ such that $v(r) = (r/r_b)v_b$ where v_b is given by Eq. 5 in the manuscript. Using this simple flow field approximation, we obtain an expression for p_y^+ developed during the bridge formation phase of droplet coalescence ($r_b/R < 1$),

$$p_y^+\big|_{r_b/R \lesssim 1} = \rho \int_0^{r_b} \int_0^{\pi} rxv \sin\beta \, d\beta dr = \frac{1}{4}\rho r_b^3 C^2 \sqrt{\frac{\gamma}{\rho R}}.$$

<div align="right">Eq. S4</div>

By non-dimensionalizing Eq. S4 by the characteristic momentum of the system, $m_j U$, we can observe that the bridging flow momentum follows a volumetric scaling, $p_y^+/m_j U \sim (r_b/R)^3$.

S8. $p_y^+\big|_{r_b/R=2^{1/3}}$ CONTRIBUTION TO JUMPING DROPLET MOMENTUM
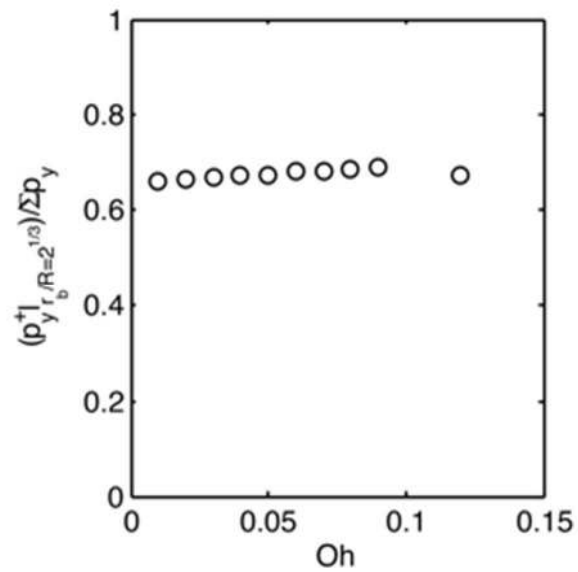
Figure S8 – Contribution of the *y*-component of momentum generated in upper half of the coalescing droplets $(p_y^+\big|_{r_b/R=2^{1/3}})$ relative to the total momentum driving droplet jumping as a function of *Oh* evaluated from the numerical simulations. The results indicate an average contribution of 0.67.

S9. FIT STATISTICS TO NUMERICAL v_j/U DATA
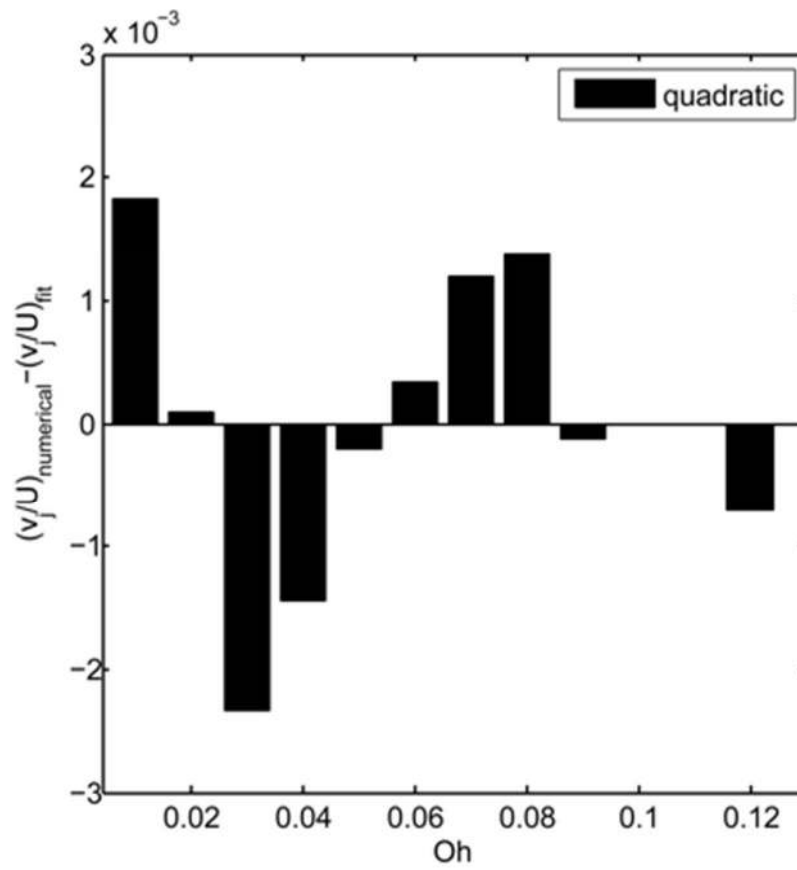
Figure S9 – Residuals of quadratic fit given by $v_j/U = 3.4026Oh^2 - 1.5285Oh + 0.2831$ to the numerical v_j/U data obtained from Fig. 5d. The norm of the residuals was $3.8467x10^{-3}$.

S10. CONVERTED ENERGY CALCULATION

The jumping speed is given by

$$v_j = DU = D\sqrt{\frac{\gamma}{\rho R}},$$

Eq. S5

where $D = 3.4026Oh^2 - 1.5285Oh + 0.2831$ (Figure 5d), ρ is the liquid density and R is the radius of the two equally-sized droplets prior to coalescence. The mass of the jumping droplet is

$$m_j = \frac{8}{3}\rho\pi R^3.$$

Eq. S6

From Eq. S5 and Eq. S6, we can calculate the kinetic energy of the jumping droplet as

$$E_j = \frac{1}{2}m_j v_j^2.$$

Eq. S7

Next, we calculate the excess surface energy released during the coalescence process for two, equally-sized droplets in the limit that $\theta_a^{app} \to 180°$,

$$\Delta E = E_1 - E_2 = 8\gamma\pi R^2 - 4\gamma\pi\left(2^{1/3}R\right)^2.$$

Eq. S8

We define the energy conversion efficiency of the process by taking the ratio of Eq. S7 and Eq. S8,

$$\eta_j = \frac{E_j}{\Delta E} = \frac{D^2}{3\left(2 - 2^{2/3}\right)}.$$

Eq. S9

Figure S10 plots Eq. S9 as a function of D. We see that as D decreases (increasing Oh), the amount of excess surface energy transferred to the kinetic energy of the jumping droplet decreases quadratically, reducing from ~6% at $D \approx 0.28$ ($Oh \to 0$) down to ~1.8% at $D \approx 0.15$ ($Oh = 0.12$).
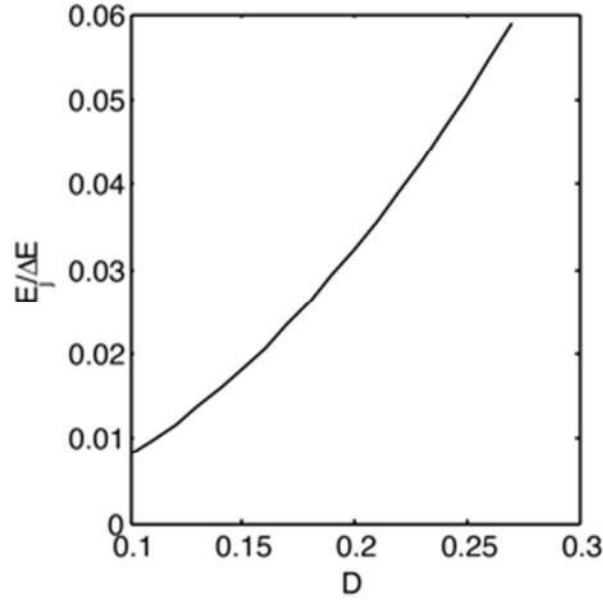
Figure S10 – Fraction of excess surface energy converted to the kinetic energy of the jumping droplet as a function of the *Oh* dependent pre-factor, *D*, in Eq. S5 for the coalescence of two, equally sized droplets the limit that $\theta_a^{app} \to 180°$.

S11. INDEPENDENCE OF JUMPING VELOCITY ON GASS PRESSURE
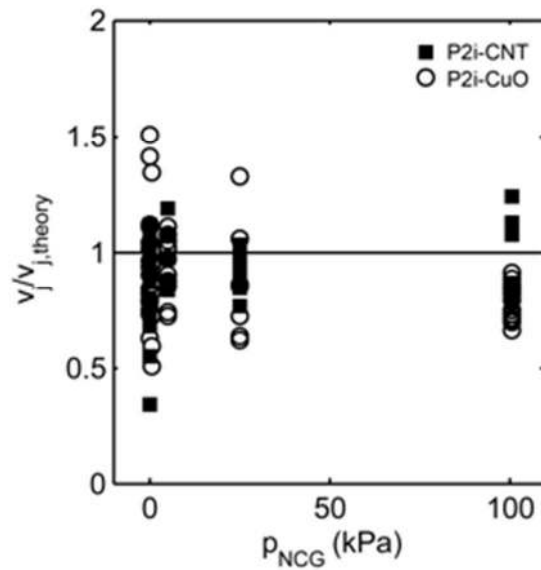
Figure S11 – Experimental jumping velocities normalized by the theoretical predictions (Eq. 10) plotted as a function of non-condensable gas pressure (p_{NCG}) in the environmental chamber. A linear fit to the P2i-CuO sample data gives a slope of m = -1.33x10-3 with a norm of the residuals of 1.45. A linear fit to the P2i-CNT sample data gives a slope of m = 6.87x10-4 with a norm of the residuals of 1.12. Despite the scatter, the data does not suggest that the jumping velocity is dependent on the surrounding pressure of the gas.

Supplemental references

(1)   Boreyko, J. B.; Chen, C.-H. Vapor Chambers with Jumping-Drop Liquid Return from Superhydrophobic Condensers. *Int. J. Heat Mass Transf.* **2013**, *61*, 409–418.

(2)   Miljkovic, N.; Preston, D. J.; Enright, R.; Wang, E. N. Electric-Field-Enhanced Condensation on Superhydrophobic Nanostructured Surfaces. *ACS Nano* **2013**, *7*, 11043–11054.

(3)   Lecoq, N.; Anthore, R.; Cichocki, B.; Szymczak, P.; Feuillebois, F. Drag Force on a Sphere Moving Towards a Corrugated Wall. *J. Fluid Mech.* **2004**, *513*, 247–264.

(4)   Miljkovic, N.; Preston, D.; Enright, R.; Wang, E. N. Electrostatic Charging of Jumping Droplets. *Nat. Commun.* **2013**, *4*, 2517, doi:10.1038/ncomms3517.

(5)   Feng, Z.-G.; Michaelides, E. E. Drag Coefficients of Viscous Spheres at Intermediate and High Reynolds Numbers. *J. Fluids Eng.* **2001**, *123*, 841–849.

(6)   Stone, H. A. Dynamics of Drop Deformation and Breakup in Viscous Fluids. *Annu. Rev. Fluid Mech.* **1994**, *26*, 65–102.

(7)   Paulsen, J. D.; Burton, J. C.; Nagel, S. R. Viscous to Inertial Crossover in Liquid Drop Coalescence. *Phys. Rev. Lett.* **2011**, *106*, 114501.

(8)   Duchemin, L.; Eggers, J.; Josserand, C. Inviscid Coalescence of Drops. *J. Fluid Mech.* **2003**, *487*, 167–178.